International Journal of Solids and Structures 47 (2010) 2918–2936

Contents lists available at ScienceDirect

International Journal of Solids and Structures

journal homepage: www.elsevier.com/locate/ijsolstr

Amplitude dependence of filler-reinforced rubber: Experiments, constitutive modelling and FEM – Implementation

Martin Rendek *, Alexander Lion **

Institute of Mechanics, Department of Aerospace Engineering, University of Federal Armed Forces, Munich, Germany

ARTICLE INFO

Article history:
Received 15 September 2009
Received in revised form 4 May 2010
Available online 30 June 2010

Keywords:
Payne effect
Process dependency
Dynamic material properties
Finite viscoelasticity
USERMAT
Harmonic simulations

ABSTRACT

The focus of the present paper is the experimental investigation, the constitutive representation and the numerical simulation of the amplitude dependence of filler-reinforced elastomers. A standard way to investigate the dynamic properties of viscoelastic materials is via the dynamic modulus which is obtained from stress signals due to harmonic strain excitations. Based on comprehensive experimental data, an amplitude-dependent constitutive model of finite viscoelasticity is developed. The model is based on a modified Maxwell chain with process-dependent viscosities which depend on additional internal state variables. The evaluation of this thermodynamically consistent model is possible in both the time domain, via stress-time signals, and in the frequency domain, via the dynamic modulus. This property is very profitable for the parameter identification process. The implementation of the constitutive model into the commercial finite element code ANSYS with the user-programmable feature (UPF) USERMAT for large deformations in updated Lagrange formulation is presented. This implementation allows simulating the time-dependent behaviour of rubber components under arbitrary transient loading histories. Due to physical and geometrical nonlinearities, these simulations are not possible in the frequency domain. But, transient FEM computations of large loading histories are sometimes not possible in an acceptable time. In the context of the parameter identification the fundamental ideas are presented, how this problem has been solved. Transient FEM simulations of real rubber components are also shown to visualize the properties of the model in the context of the transient material behaviour.

1. Introduction

Rubber-parts which are manufactured using filler-reinforced elastomers are used in many industrial applications (Sjöberg, 2002; Coja and Kari, 2005). The most popular and best-known ones come from the automotive industry and contain shock absorbers (Garcia, 2006), suspension and engine mounts, tyres, seals or belts for transmitting power, to name a few. In order to improve and modify the physical properties of rubber-like materials, a wide range of fillers like silica or carbon black is used (Heinrich and Klüppel, 2004). The addition of appropriate filler particles to the elastomers leads to additional cross-links and usually influences the behaviour of the final product in a positive sense: increase in stiffness and abrasion resistance or advances in the adhesion behaviour of tyres (Bokobza, 2009). On the other hand, the added filler material can cause complications during the production process. The particles tend to agglomerate during mixing such that the resulting material can become rather inhomogeneous. To avoid this, further chemical additives are needed.

Under real operating conditions, typical rubber components are loaded with complicated dynamic processes in combination with constant preloads. During oscillating deformations, filled rubber shows many nonlinear effects which are a result of the dynamic breakage and recovery of the additional cross-links in the network. On the level of the material, dynamic loadings can be generated and studied using the experimental technique of dynamic mechanical analysis (DMA). In this context, continuous changes or jumps in the frequency (G'Sell and Jonas, 1981), the temperature (Khan and Lopez-Pamies, 2002; Williams et al., 1955; Schwarzl and Zahradnik, 1980), the static preload and the dynamic amplitude (Payne, 1962a,b) are applied. Well-known inelastic phenomena of filler-reinforced rubber are the frequency- and the amplitude-dependence (Payne-effect) as well as the stress softening behaviour under large cyclic strains which is known as the Mullins-effect (Buche, 1961; Hardwood et al., 1965; Mullins and Tobin, 1965). In addition, jamming phenomena are observed as a reason of loading history and amplitude dependence (Robertson and Wang, 2005, 2006). The dynamic material properties of rubber under multi-modal loading processes, which are very similar to real operating

* Corresponding author. Tel.: +49 89 6004 2124; fax: +49 89 6004 2386.
** Corresponding author. Tel.: +49 89 6004 2494; fax: +49 89 6004 2386.
E-mail addresses: martin.rendek@unibw.de (M. Rendek), Alexander.Lion@unibw.de (A. Lion).

0020-7683/$ - see front matter © 2010 Elsevier Ltd. All rights reserved.
doi:10.1016/j.ijsolstr.2010.06.021

Nomenclature

$\mathbf{A}$	tensors
det$\mathbf{A}$	determinant of $\mathbf{A}$
$\mathbf{A}^T$	transpose of $\mathbf{A}$
$\mathbf{A}^D$	deviator of $\mathbf{A}$
$\mathbf{F}$	deformation gradient
$\mathbf{C} = \mathbf{F}^T\mathbf{F}$	right Cauchy–Green tensor
$\mathbf{B} = \mathbf{F}\mathbf{F}^T$	left Cauchy–Green tensor
$\mathbf{U} = \sqrt{\mathbf{C}}$	right stretch tensor
$\mathbf{V} = \sqrt{\mathbf{B}}$	left stretch tensor
$\mathbf{R}$	rotation tensor
$\mathbf{E} = \frac{1}{2}(\mathbf{C} - \mathbf{1})$	Green strain tensor
$\mathbf{A} = \frac{1}{2}(\mathbf{1} - \mathbf{B}^{-1})$	Almansi strain tensor
$\mathbf{e} = \frac{1}{2}(\mathbf{C}^{-1} - \mathbf{1})$	Piola strain tensor
$\mathbf{a} = \frac{1}{2}(\mathbf{1} - \mathbf{B})$	Finger strain tensor
$\mathbf{T}$	Cauchy stress tensor
$\mathbf{S} = (\det\mathbf{F})\mathbf{T}$	Kirchhoff stress tensor
$\mathbf{T}_{PK} = \mathbf{S}\mathbf{F}^{T-1}$	first Piola–Kirchhoff stress
$\widetilde{\mathbf{T}} = \mathbf{F}^{-1}\mathbf{T}_{PK}$	second Piola–Kirchhoff stress
ψ	specific free energy per unit mass
ρ_R	mass density
θ	thermodynamic temperature
s	specific entropy per unit mass
$\mathbf{q}_R$	heat flux vector
J	volume ratio
$\mathbf{B}_l$	matrix connecting the changes in the linear strain $\delta\mathbf{e}_l$ and the nodal displacement vector δp
$\widetilde{\mathbb{C}}$	material tangent operator – tensor of fourth order
$\mathbf{G}$	matrix connecting the displacement derivates to the nodal displacements
$\widehat{\mathbf{T}}$	matrix containing the Cauchy stress
$\mathbf{F}^{-1}(\circ)\mathbf{F}^{T-1}$	'push forward' transformation
$\mathbf{F}(\circ)\mathbf{F}^T$	'pull back' transformation
$(\circ)_R$	entity in the reference coordinate system
$(\circ)_C$	entity in the current coordinate system
$\mathbf{L}=\mathbf{D}+\mathbf{W}=\dot{\mathbf{F}}\mathbf{F}^{-1}$	spatial velocity gradient
$\mathbf{D}=\frac{1}{2}(\mathbf{L}+\mathbf{L}^T)=\mathbf{D}^T$	symmetric part of velocity gradient
$\mathbf{W}=\frac{1}{2}(\mathbf{L}-\mathbf{L}^T)=-\mathbf{W}^T$	antisymmetric part of velocity gradient
$\Delta\mathbf{F}$	incremental deformation gradient, $\mathbf{F}(t+\Delta t) = \Delta\mathbf{F}\mathbf{F}(t)$
$\Delta\mathbf{H}$	incremental displacement gradient
$\Delta\mathbf{L}$	incremental velocity gradient
$\Delta\mathbf{D}$	symmetric part of incremental velocity gradient
$\Delta\mathbf{W}$	skew-symmetric part of incremental velocity gradient
$\Delta\mathbf{R}$	incremental rotation tensor
$t,\Delta t$	time and time increment
ω	angular frequency

conditions, were measured and presented in Wrana and Härtel (2008). In order to understand these effects in more detail it is profitable to execute cyclic DMA tests with complicated amplitude histories. Besides the standard DMA tests and the interpretations via the dynamic modulus it is very helpful to record also the stress and strain signals as function of time. This data allows observing further transient effects and gives more insight into the dynamics of the material.

The focus of this paper is concentrated to the amplitude dependence of rubber which was originally observed in the sixties (Payne, 1962a,b). In comparison with the Mullins-effect which occurs under large strain amplitudes, the Payne-effect takes place under small strain amplitudes. If filler-reinforced rubber is cyclically deformed the Payne-effect comes to light in the form of a monotonically decreasing storage modulus and a sigmoidal-shaped loss modulus with increasing strain amplitude. On a molecular level, the Payne-effect can be attributed to dynamic reversible breakdown and recovery processes of carbon black aggregate structures (Payne and Whittaker, 1972). The influence of diverse parameters like temperature, frequency or the degree of vulcanization on the Payne-effect was studied in many publications. Constitutive models to represent the amplitude dependence of filled rubber were published, for example, in Lion (2005) and Hoefer and Lion (2009), or in Lion (2004) and Dorfmann and Be'ersheba (1995) considering fractional derivates. These approaches can be interpreted as time domain formulations of the well-known Kraus model (Kraus, 1966; Lion, 2005). The Kraus model describes the amplitude dependence of the dynamic modulus in the frequency domain but a time domain formulation which can be applied, for example, for finite element simulations of rubber parts does not exist. Another interesting approach, the network junction model, was introduced by Ouyang (2006) in this context. The formulation and the finite element implementation of a constitutive model which can take the amplitude dependence in both the frequency and the time domain into account is the topic of this paper.

Since the equilibrium hysteresis of filled elastomers is comparatively small (Lion, 1996), their behaviour under infinitely slow processes is nonlinear elastic in a good approximation. If stress- or strain-controlled loadings with different rates are applied filled elastomers exhibit a pronounced rate-dependent behaviour. This can be observed in the form of creep and relaxation curves or rate-dependent stress–strain characteristics. The relaxation can be observed during dynamic loadings too (Sullivan and Demery, 1982). The foundations of linear viscoelasticity on the basis of the Boltzmann formulation were published, for example, by Coleman (1961). Rheological constitutive models to represent the nonlinear viscoelastic behaviour of rubber can be found in many publications, for example, Baris and Edwards (1993), Hasanpour et al. (2009), Haupt and Lion (2002), Holzapfel (1996), Middendorf (2001) or Miehe and Keck (2000), Sedlan (2001), Amin et al. (2006) to name a few. Numerical aspects of the finite element implementation of finite viscoelasticity are discussed, for example, by Simo and Huges (2000) and Reese and Govindjee (1998) or Miehe and Keck (2000) and Govindjee and Simo (1992).

In the first section of the paper, dynamic tests on filled and unfilled rubber are presented. Transient effects are evaluated and discussed in both the frequency and the time domain. In the subsequent section, a general model of nonlinear finite viscoelasticity with process-dependent viscosities is developed. Variable viscosities are introduced to take the amplitude dependence into account. In order to illustrate the idea of the model, one-dimensional MATLAB simulations are carried out. In the Section 3, the constitutive model with a nearly incompressible hyperelastic equilibrium stress and a rate-, frequency- and amplitude-dependent overstress is formulated. The implementation of the constitutive model into the finite element code ANSYS via the subroutine USERMAT is explained and the co-rotational kinetics of this formulation is discussed too. In Section 6, the material model is geometrically linearised and transformed into the frequency domain in order to identify certain material parameters. The scaling process of the time in the context of the transient processes is shortly discussed. Finally, some transient FEM simulations to demonstrate the abilities of material model are shown and interpreted.

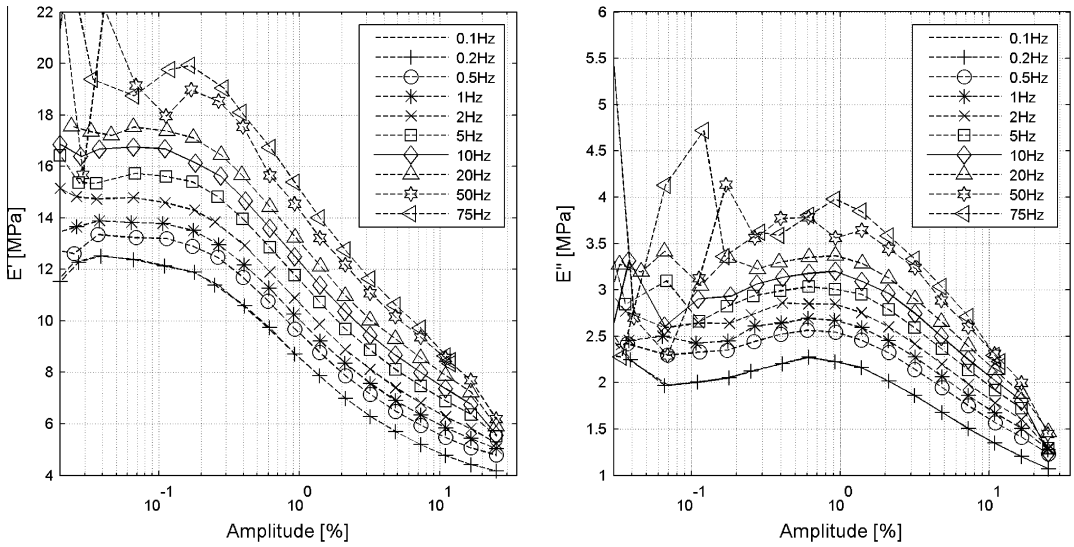

Fig. 1. Frequency- and amplitude-dependence of Payne-effect; storage (L) and loss (R) modulus of filled ESBR with 50 phr carbon black.

2. Experiments on filler-reinforced rubber compounds

As a standard approach to investigate the Payne-effect (amplitude dependence), strain-controlled amplitude sweep tests were carried out (Fig. 1). In these tests, the amplitude of a sinusoidal strain excitation under constant preload and frequency is continuously varied. The experiments were carried out with a DMA (Dynamic Mechanical Analysis) testing machine, repeated for different frequencies and evaluated in terms of the storage and loss moduli. The storage modulus determines that part of the stress response which is in phase with the strain and the loss modulus that part which is in phase with the strain rate. The experimental data shows the transient region of the amplitude-dependent storage and loss modulus of carbon black-filled rubber at different frequencies. The curves of the storage modulus decrease significantly with increasing strain amplitude (Fig. 1-L).

In comparison with this, the loss modulus shows a broad maximum in the region of intermediate amplitudes (Fig. 1-R). In the region of extremely small or large strain amplitudes, the material exhibits amplitude-independent dynamic moduli or plateau areas. The experimental observation of plateau areas of the Payne-effect can also be found in Lion et al. (2009). In the current work, we concentrate the focus on the transient areas. With increasing frequency the softening effect is more pronounced because the material is stiffer and more sensitive (Rendek and Lion, 2008). Corresponding to the smallest amplitude, the frequency dependence is studied in more detail later when the material parameters are identified. The experiments in Fig. 1 show a pronounced stiffening of the material with increasing frequencies, cf. Wrana et al. (2000) or Ramorino and Ricco (2003). For comparison with filled ESBR, the same amplitude sweep at different frequencies was carried out with unfilled natural rubber (NR). It is plotted in Fig. 2 and shows an amplitude-independent dynamic modulus and weak frequency dependence. These tests demonstrate that the amplitude dependence of elastomers can be attributed to the filler or to interactions between the filler and the rubber matrix. The frequency dependence is influenced by the filler as well.

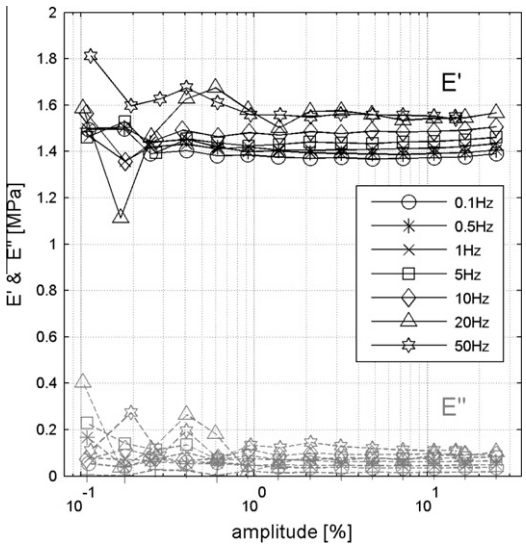

Fig. 2. Amplitude-independent behaviour of unfilled NR, storage and loss modulus.

2.1. Reversibility of Payne-effect

The next point of discussion is the difference in the material behaviour during increasing and decreasing amplitude changes which can be observed in amplitude sweeps driven in increasing and decreasing mode related to the dynamic amplitude (see Figs. 3 and 4).

As we see in Fig. 4, the dependence of the material behaviour on the loading path is relevant in the investigated deformation range above 0.1%. The differences in the values of the storage and loss modulus during increasing and decreasing strain amplitudes are caused by the loading history and the internal dynamics of the material. This effect is more pronounced in the storage modulus but less pronounced in the loss modulus. Increasing and decreasing amplitude sweeps build one loading cycle (Fig. 3-L). Between the loading cycles, hold times of 900 s are introduced to allow a regeneration of the microstructure. The value of 900 s was found to be sufficient such that the regeneration under tension is nearly complete. The values of the dynamic modulus during the first cycle are significantly bigger than those during the second and the following cycles (Fig. 4). This type of cyclic softening behaviour is very similar to that of the Mullins-effect (Mullins and Tobin, 1965) and occurs only at virgin rubber specimens. The cycles from 2 to 5 show the same curves of dynamic modulus and, thus, prove the reversibility of the Payne-effect. Nevertheless, it should be remarked that the amplitude dependence is different during increasing and decreasing amplitudes: during the amplitude increase, the modulus is observed to be larger than during the decrease. During the increase of the

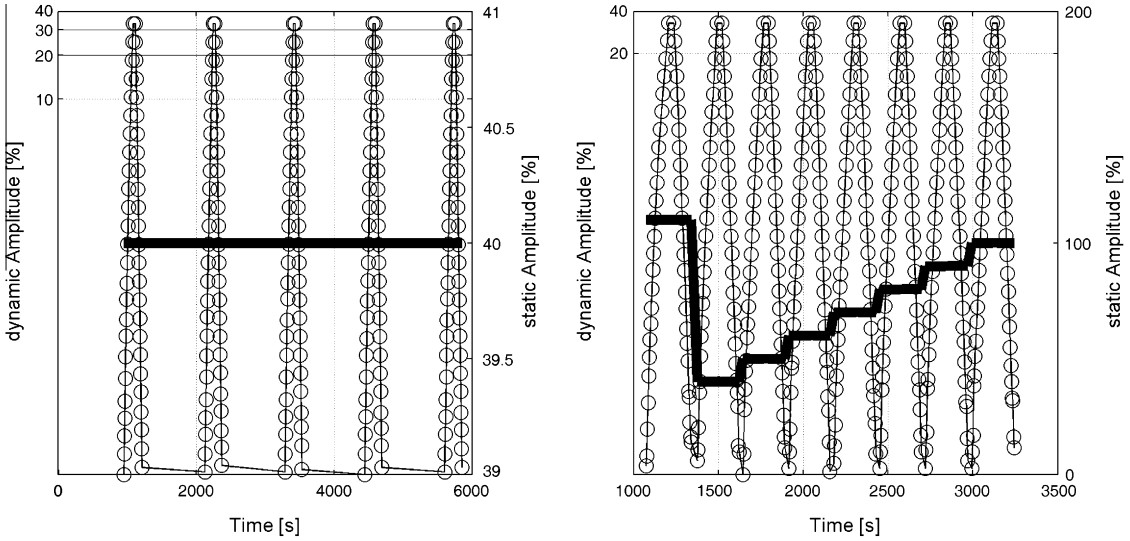

Fig. 3. Prescribed dynamic loadings (amplitude sweeps) as functions of time to determine the reversibility of the Payne-effect with constant preload and hold times (L), up- and down-sweep test with stepwise changing preload (R).

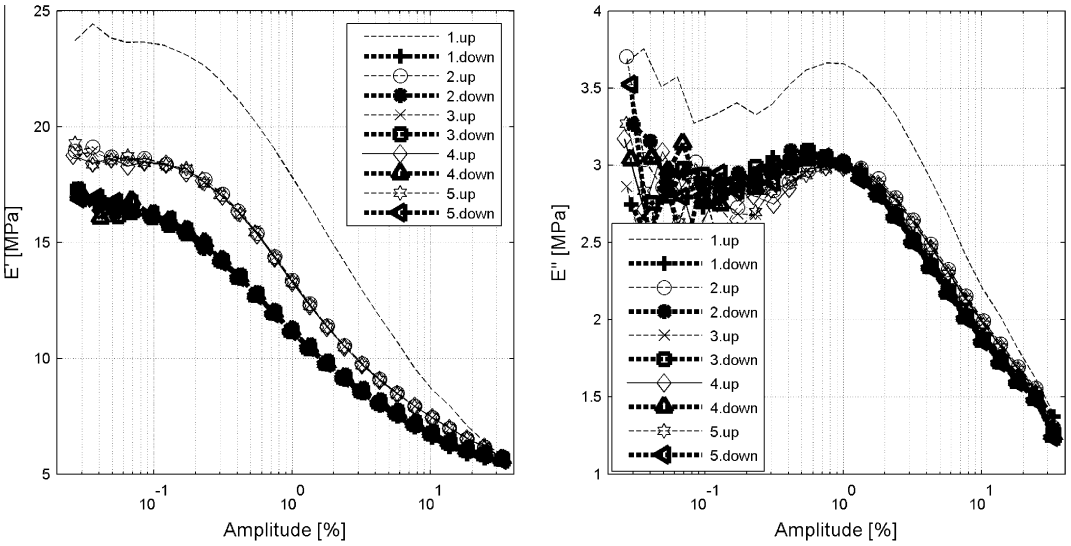

Fig. 4. Reversibility of the Payne-effect, storage (L) and loss (R) modulus of filled ESBR with 50 phr carbon black under constant preload as plotted in Fig. 3-L.

amplitude, the weakest physical bonds are breaking instantaneously and during the decrease they recover with a temporal delay.

2.2. Influence of preload

In order to determine the influence of the static preload on the Payne-effect, amplitude sweeps at different preloads were carried out. The loading process is depicted in Fig. 3-R. Fig. 5 shows the response of the dynamic modulus belonging to the sweeps with increasing amplitudes. The first sweep is not considered because it was done to precondition the specimen. The curves of the storage modulus in Fig. 5 exhibit a significant influence on the preload in the full range of strain amplitudes. Growing preloads produce larger stress amplitudes which are directly transferred to the dynamic modulus. The sensitivity of the loss modulus to the preload is less pronounced and can be ignored in a first approximation.

2.3. Observation of the Payne-effect in time domain

In order to investigate the amplitude dependence of filled elastomers, i.e. the reversible softening behaviour of the dynamic modulus under growing strain amplitudes (Payne, 1965), cyclic DMA tests under harmonic tension, shear or compression deformations are usually carried out. Mostly, the experimental data are evaluated in the frequency domain in terms of the dynamic modulus. In this case, both the higher frequency contributions which are caused by geometrical or physical nonlinearities and the transients in the response of the material are not observable. Thus, in addition to the behaviour in the frequency domain the present section is focussed to the time-dependent behaviour of the stress and strain signals recorded during the DMA tests (Fig. 1).

Fig. 6 shows the signals during the amplitude sweep at a frequency of 60 Hz. Prior to the real tests, the specimens were conditioned to eliminate the Mullins-effect. For the sake of brevity, the mechanical conditioning process is not plotted. It is observed, that the stress amplitudes decrease significantly during a certain time after the amplitude change. The material which is deformed in such a way becomes softer with increasing amplitudes which corresponds to the Payne-effect in the time domain. The observed softening and recovery effects can be physically interpreted as process-induced reversible changes in the microstructure of the material. The influences of the excitation frequency on the

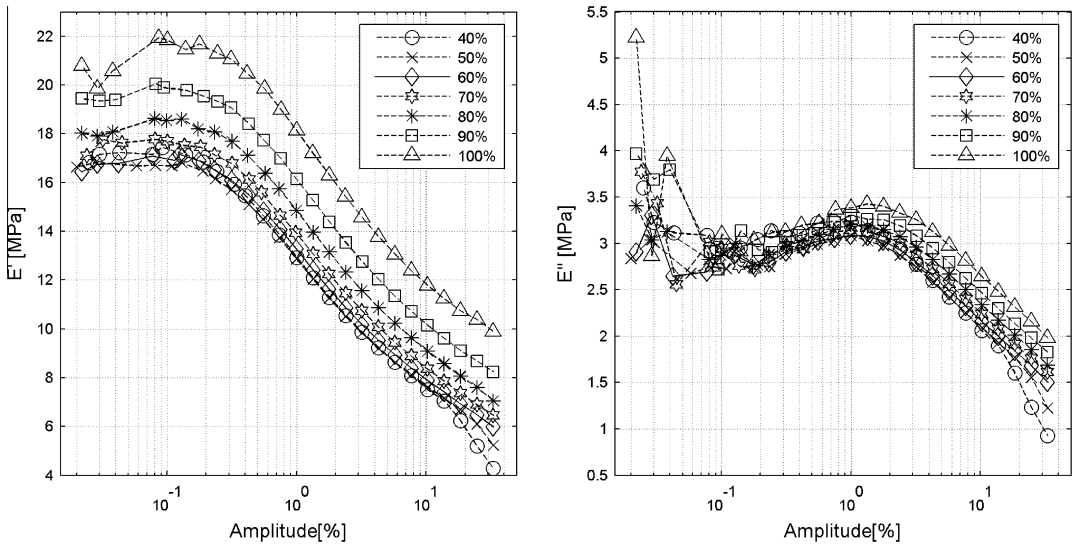

Fig. 5. Influence of the preload on the Payne-effect, storage (L) and loss (R) modulus of filled ESBR with 50 phr carbon black. The loading is plotted in Fig. 3-R.

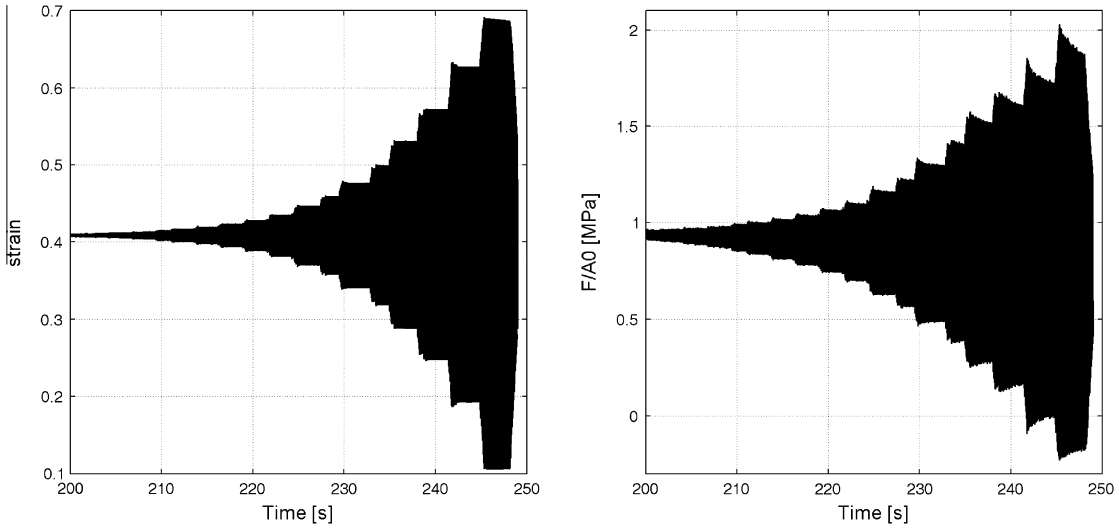

Fig. 6. Recorded tensional strain signal (L) and stress response (R) of filled reinforced ESBR by standard amplitude sweep test at 60 Hz and 25 °C.

microstructural relaxation behaviour and the intensity of the stress softening are studied in Fig. 6-R and Fig. 7-L. In comparison with the stress signal of filed ESBR (Fig. 7-L), unfilled NR (Fig. 7-R) exhibits completely different behaviour: the stress amplitudes of unfilled NR are constant after the amplitude changes.

The amplitude-dependent softening effect is also detectable on the stress–strain hysteresis loops. In Fig. 8, the hysteresis loops belonging to the stress signals in Fig. 7 are plotted as functions of strain. The dynamic stiffness, defined as the average slope of the hysteresis loops, varies with the strain amplitude and is growing with decreasing amplitude. This phenomenon is particularly pronounced in the case of carbon black-reinforced ESBR (Fig. 8-L). Unfilled rubber shows clear hyperelastic behaviour (Fig. 8-R).

2.4. DMA multi-step experiments

Another method to study the Payne-effect in the time domain is a multi-step test. It consists of a sequence of time intervals of sufficiently long duration in which the strain amplitude is constant. During the standard amplitude sweep the hold times at constant strain amplitudes are definitely too small. In the following tests, the amplitude is constant for 2700 s and then changes. Looking at the corresponding stress signals in Fig. 6-R, it is observed that the microstructure relaxations are definitely not finished. As a result of the multi-step test in Fig. 9, the amplitude-dependent dynamic modulus is a time-dependent function. In the region of increasing strain amplitudes (left of centre in Fig. 9-L and -R), the dynamic modulus has become constant after relative short times and its asymptotic values become stepwise smaller. But in the region of decreasing amplitudes (right of centre in Fig. 9-L and -R) the relaxation of the modulus is not finished for the smaller strain amplitudes and its end values raise stepwise. The benefit of this test is to get the information about finished or unfinished microstructural relaxations after the amplitude jumps. The stationary values of the dynamic modulus obtained from the multi-step test in Fig. 9 match with the modulus values belonging to the same strain amplitude and frequency (10 Hz) from the amplitude sweep test in Fig. 1. The effect of the loading path dependence (see Fig. 4) which has been cleared in Section 2.3 is observed in the area of small dynamic amplitude too. Differences in the stationary values of the dynamic modulus at the same dynamic amplitude at the start and the end

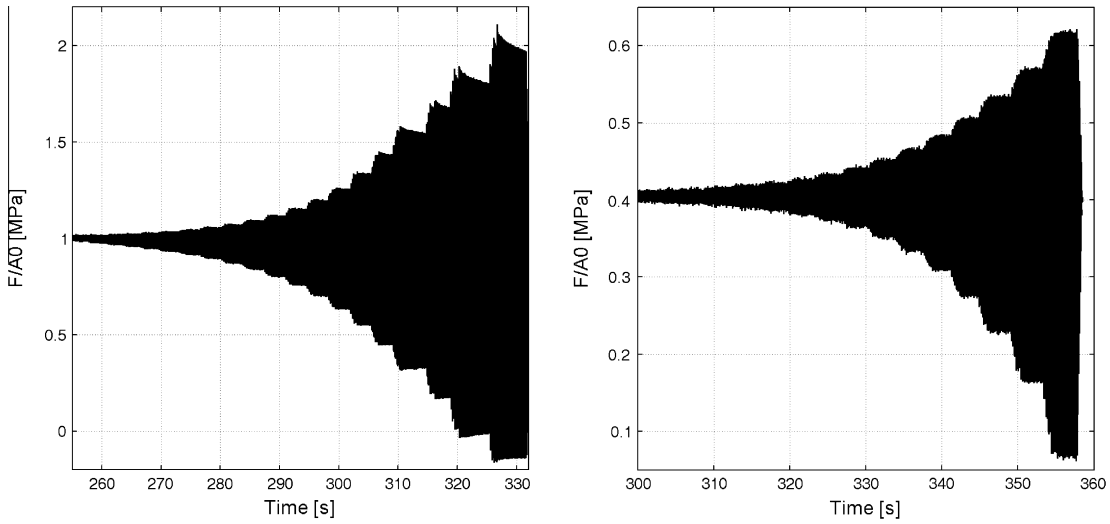

Fig. 7. Recorded tensional stress response of carbon black-filled ESBR (L) and unfilled NR (R) at 10 Hz and 25 °C from standard amplitude sweep test.

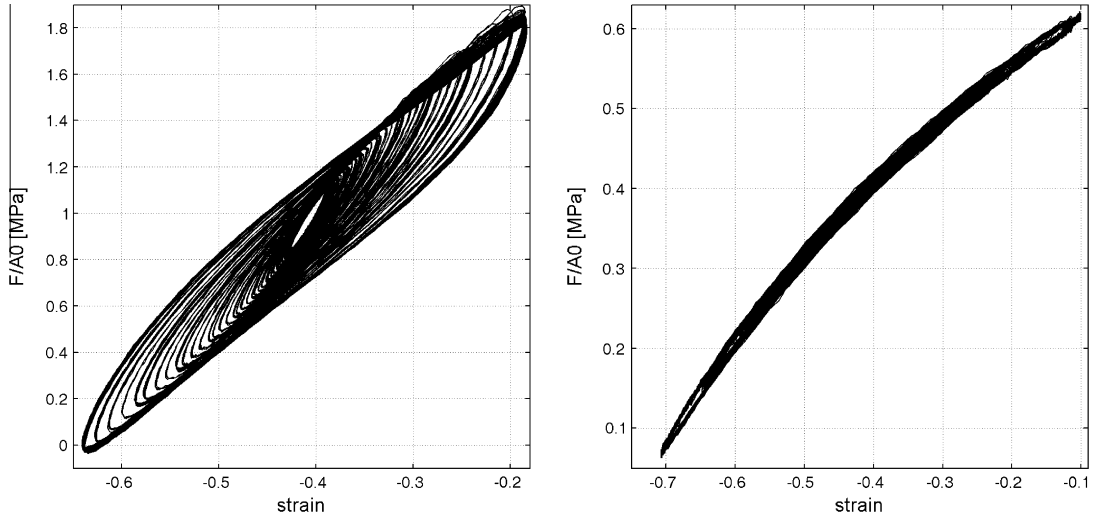

Fig. 8. Hysteresis loops from standard amplitude sweep tests at 10 Hz, carbon black-filled ESBR (L) and unfilled NR (R).

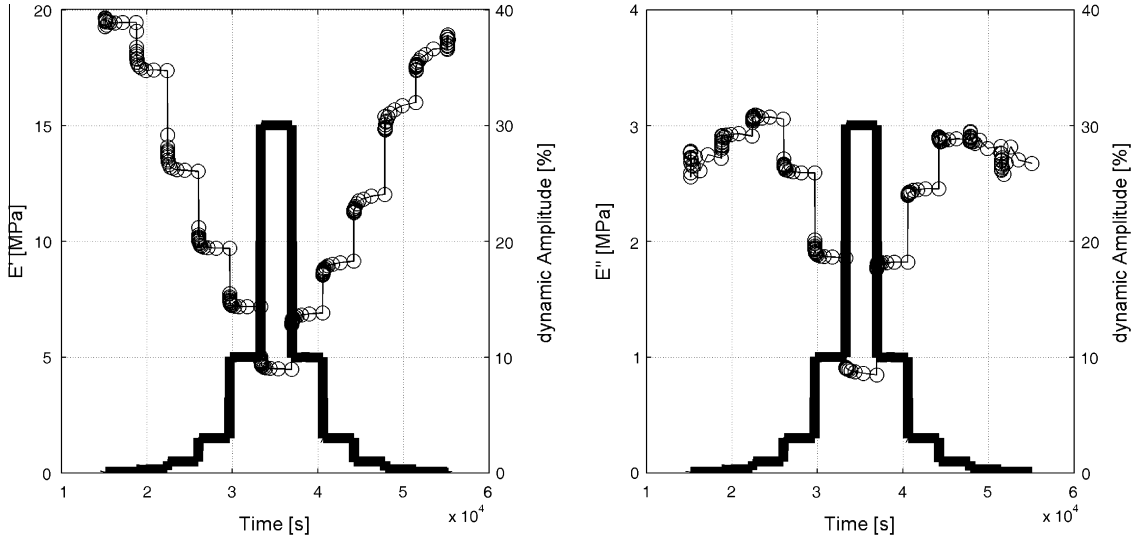

Fig. 9. Multi-step tension test at 10 Hz on carbon black-filled ESBR, storage modulus (L) and loss modulus (R). The fat curves represent the strain amplitude as function of time.

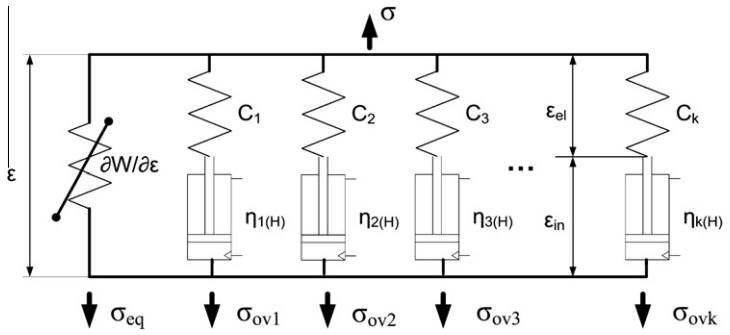

Fig. 10. 1D Maxwell chain with process-dependent viscosities and nonlinear equilibrium stress.

of the tests can be interpreted as loading path history influence of the material.

3. Constitutive modelling based on finite viscoelasticity

Besides the phenomena presented in the previous section, rubber-like materials also exhibit pronounced hyperelastic behaviour under large quasistatic deformations and viscoelastic behaviour (e.g. creep, relaxation and rate-dependent stress–strain curves) under time-dependent loading processes. The concept of finite nonlinear viscoelasticity which is based on three-dimensional Maxwell elements provides a good basis for the constitutive representation of the experimentally observed phenomena. Examples, based on this or similar concepts, can be found by Coleman (1961), Reese and Govindjee (1998), Holzapfel (1996), Simo and Huges (2000) or Liu (2007), Laiarinandrasanaa et al. (2003). In order to consider further nonlinear effects it is convenient to extend the constitutive models with additional internal variables. In the case of viscoelastic media, process-dependent viscosities are frequently introduced (Haupt and Lion, 2002; Lubliner, 2006). Maxwell element-based approaches modified in such a way were successfully applied to simulate the Payne-effect in the frequency domain with good agreement to experimental data by Hoefer and Lion (2009) or, earlier, by Lion (1996). Another, but similar, concept which uses internal variables and fractional differential equations to simulate the Payne-effect is presented in Lion and Kardelky (2004). The influence of the preload on the Payne-effect is neglected in this paper because this effect becomes more significant, if the static deformation is larger that about 60% (Fig. 5). A constitutive approach which considers this influence can be found, for example, in. Ji-Hyun Cho (2006) and Suwannachit and Nackenhorst (2010).

3.1. One-dimensional amplitude-dependent Maxwell chain

In order to formulate the three-dimensional constitutive model for finite deformations, the main ideas are motivated in the following discussion on the basis of a one-dimensional approach. The framework of a one-dimensional amplitude-dependent Maxwell chain is depicted in Fig. 10, in which the total stress is decomposed into the sum of a rate-independent equilibrium stress and a rate-dependent overstress (Eq. (1)). The nonlinear hyperelastic material behaviour is considered in the equilibrium stress and the viscoelastic behaviour in the overstress. The amplitude dependence is taken into account with process-dependent viscosities of the dashpots. The equilibrium stress is defined as the partial derivative of a strain energy function and depends on the total strain. The overstress is formulated as the sum of partial overstresses belonging to a series of Maxwell elements in parallel. The constitutive equations for the partial overstresses have the form of linear elastic stress–strain relations which depend on additional internal variables. This approach is sufficient to describe the experimental data, because the strain amplitudes acting on the springs of the Maxwell elements remain relatively small during dynamic excitations.

$$\sigma = \sigma_{eq} + \sum_{k=1}^{n} \sigma_{ovk} = \rho_R \frac{\partial \psi}{\partial \varepsilon} + \sum_{k=1}^{n} c_k(\varepsilon - \varepsilon_{ink}) \tag{1}$$

The elastic strains of the Maxwell elements are given by the differences between the total strain and the inelastic strains belonging to the dashpots. The constitutive equations for the inelastic strains will be derived from the Clausius–Duhem inequality.

3.2. Process-dependent inelastic strain and thermodynamical consistency

As a general rule, rheological-based constitutive models are thermodynamically consistent for arbitrary deformation processes and the evaluation of the Clausius–Duhem inequality can be used to derive the evolution equations for the inelastic strains or other internal state variables. For the Maxwell chain sketched in Fig. 10, the stored free energy, see, e.g. Krawietz (1986), can be written as expressed by Eq. (2):

$$\rho_R \psi = \rho_R \psi_{eq} + \rho_R \psi_{ov} = \left(\frac{1}{2} E \varepsilon^2 + \sum_{k=1}^{n} \frac{1}{2} c_k (\varepsilon - \varepsilon_{ink})^2 \right) \tag{2}$$

The one-dimensional form of the Clausius–Duhem inequality, abbreviated as CDI, is defined in Eq. (3). More details about the CDI and thermodynamic considerations with respect to material theory can be found in Müller (1973) or Lion (2000).

$$-\rho_R \dot{\psi} + \sigma \dot{\varepsilon} - \rho_R s \dot{\theta} - \frac{1}{\theta} q_R \cdot \nabla \theta \geqslant 0 \tag{3}$$

The quantities ρ_R, ψ, s, θ, q_R, $\nabla\theta$ are the mass density, the specific free energy and the entropy per unit mass, the thermodynamic temperature, the heat flux vector and the gradient of temperature.[1] For isothermal processes, θ = const., $\dot{\theta} = 0$, $\nabla\theta = 0$ is considered. In combination with the ansatz $\psi = \psi(\varepsilon, \varepsilon_{ink}, \ldots)$ the CDI reduces to Eq. (4):

$$\begin{aligned} &\sigma \dot{\varepsilon} - \rho_R \dot{\psi} \geqslant 0 \\ &\left(\sigma - \frac{\partial \psi}{\partial \varepsilon} \right) \dot{\varepsilon} - \sum_{k=1}^{n} \frac{\partial \psi}{\partial \varepsilon_{ink}} \dot{\varepsilon}_{ink} \geqslant 0 \end{aligned} \tag{4}$$

In the case of the rheological Maxwell chain and the free energy function as formulated in Eq. (2), the dissipation inequality leads to the following expression:

$$\left(\sigma - \left(E\varepsilon + \sum_{k=1}^{n} c_k(\varepsilon - \varepsilon_{ink}) \right) \right) \dot{\varepsilon} + \sum_{k=1}^{n} c_k(\varepsilon - \varepsilon_{ink}) \dot{\varepsilon}_{ink} \geqslant 0 \tag{5}$$

In order to satisfy Eq. (5) for arbitrary strain rates, its factor has to

[1] $\nabla\theta = Grad\theta$.

vanish such that the constitutive equation for the stress, Eq. (6), is obtained. Since the remaining terms in Eq. (5) have to be equal to or greater than zero, the expressions for the inelastic strain rates in Eq. (7) are obtained.

$$\sigma = E\varepsilon + \sum_{k=1}^{n} c_k(\varepsilon - \varepsilon_{ink}) = \sigma_{eq} + \sigma_{ov} \tag{6}$$

In combination with the process-dependent viscosities $\eta_k(H_k) > 0$, Eq. (7) leads to a non-negative dissipation and satisfies the CDI, which is the proof of the thermodynamical consistency of the constitutive model. This relation is the constitutive equation of a nonlinear dashpot.

$$\dot{\varepsilon}_{ink} = \frac{c_k}{\eta_k(H_k)}(\varepsilon - \varepsilon_{ink}) = \frac{1}{\eta_k(H_k)}\sigma_{ovk}, \quad \eta_k(H_k) > 0 \tag{7}$$

Eqs. (6) and (7) can represent the relaxation behaviour of rubber-like elastomers. In many papers, these two equations are combined to obtain one differential equation for the partial overstress:

$$\dot{\sigma}_{ovk} = c_k\dot{\varepsilon} - \frac{c_k}{\eta_k(H_k)}\sigma_{ovk} = c_k\dot{\varepsilon} - \frac{1}{Z_k}\sigma_{ovk} \tag{8}$$

Eq. (8) can be solved for η_k = const. in the form of a convolution integral.

3.3. Representation of amplitude dependence

The amplitude dependence is considered via process-dependent viscosities as given in Eq. (9):

$$\eta_k(H_k) = \frac{\eta_k^0}{H_k} \tag{9}$$

Inserting Eq. (9) into Eq. (7) and defining $Z_k = \eta_k^0/c_k$ with $\eta_k^0 = \text{const.}$ as relaxation time under very small strains of the Maxwell element, the inelastic strain rate, Eq. (10), is obtained.

$$\dot{\varepsilon}_{ink}(t) = \frac{c_k}{\eta_k(H_k)}(\varepsilon - \varepsilon_{ink}) = \frac{H_k(t)}{Z_k}(\varepsilon - \varepsilon_{ink}) \tag{10}$$

The relation between the amplitude dependence and the relaxation effects of the microstructure is modelled by the dimensionless function $H_k(t)$. It is defined by Eq. (11) and depends on the internal variable q_k which is defined by Eq. (12). The rate of the change in the dynamic modulus is controlled by the gain factors d_k.

This approach allows a scaling of transient processes and leads to reduced computation times compared to real loading times without loosing information. If $d_k = 0$ is assumed for all Maxwell elements, we have $H_k = 1$ such that the model becomes amplitude-independent.

$$H_k(t) = 1 + d_k q_k(t) \tag{11}$$

$$\dot{q}_k(t) = \frac{1}{\lambda_k}(\|\dot{\varepsilon}(t)\| - q_k) \tag{12}$$

The constants λ_k in the evolution equations for the variables q_k can be interpreted as relaxation times of the microstructure. However, the experimental data shows that the changes in the stress amplitude are faster when the strain amplitude increases than when it decreases (see Fig. 6). The same effect is observed in the multi-step test in Fig. 9. This implies that the quantity λ_k should depend on the deformation process. The amplitude dependence is driven by the absolute value of the strain rate which is very sensitive to amplitude changes (Rendek and Lion, 2009a,b). A principle numerical simulation of a multi-step test to present the amplitude dependence of the stress is plotted in Fig. 12. The loading process is depicted in Fig. 11-L. After time intervals of 30 s, stepwise increases in the strain amplitude from 1% to 20% were inserted. The right-hand side of Fig. 11 shows the evolution of the functions $H_k(t)$. In the case of harmonic strains with constant amplitude and frequency ω together with the assumption of $2\pi/\omega << \lambda_k$, we have $q_k \approx$ const. and $H_k \approx$ const.; if the strain amplitude tends to zero, $q_k \approx 0$ and $H_k \approx 1$ hold. If a process with changing amplitude is applied, the variables q_k or H_k are measures for the amplitude and control the stress response (Fig. 12-L). Mostly, the stress signal is evaluated via the dynamic modulus (Fig. 12-R); the computation of the modulus is described in detail, e.g. by Menard (1999) or Lion (2004). As it is seen, the dynamic modulus decreases with increasing strain amplitude. The same behaviour is quantitatively observed in the multi-step test (see Fig. 9).

The identification of the material parameters, E, c_k, η_k, d_k, λ_k on the basis of the formulation of the model in the frequency domain is discussed later in Section 5.

3.4. Three-dimensional finite strain formulation

The three-dimensional formulation of the constitutive model is based on Eq. (13) and motivated from the one-dimensional approach in Eq. (1). The Second Piola–Kirchhoff stress tensor which acts on the reference configuration is additively decomposed into

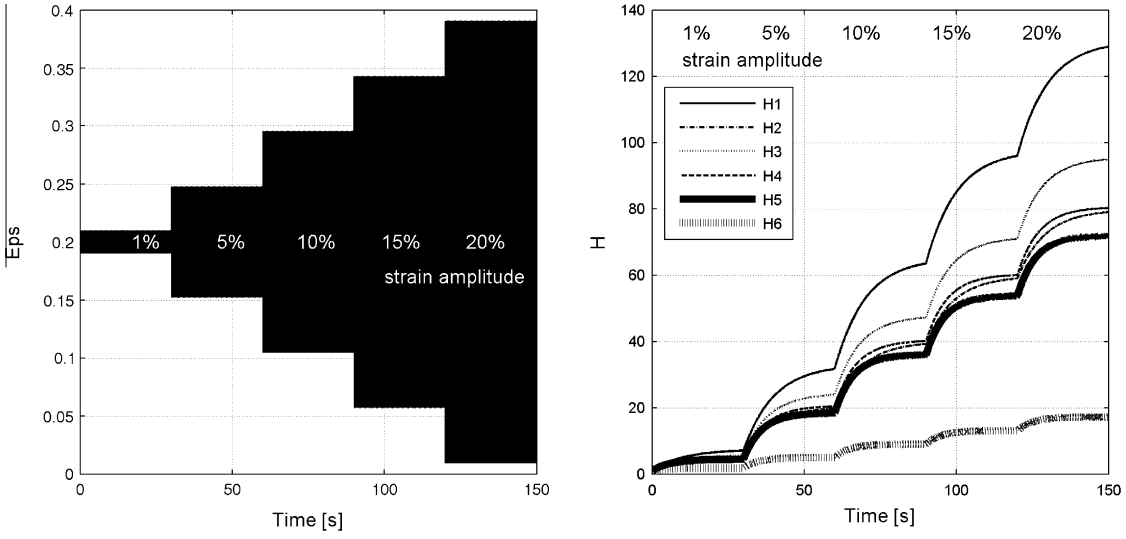

Fig. 11. Example of cyclic strain excitation with stepwise changing amplitude (L) and evolution of the functions $H_k(t)$ for each Maxwell element (R).

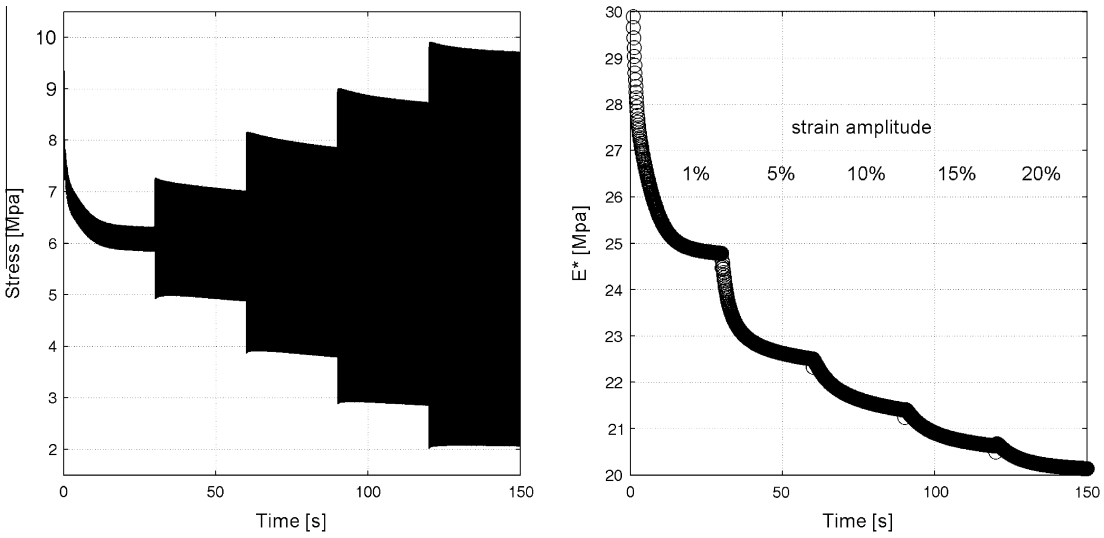

Fig. 12. Principle simulation of the amplitude-dependent stress response (L) and the computed dynamic modulus (R).

the hyperelastic equilibrium stress and the rate-dependent overstress.

$$\widetilde{\mathbf{T}} = \widetilde{\mathbf{T}}_{eq} + \sum_{k=1}^{n} \widetilde{\mathbf{T}}_{ovk} = 2\frac{\partial \psi_{eq}}{\partial \mathbf{C}} + \sum_{k=1}^{n} \widetilde{\mathbf{T}}_{ovk}(\mathbf{e}, \mathbf{e}_{ink}) \tag{13}$$

3.5. Compressible hyperelastic equilibrium stress response

The equilibrium stress is described by a nearly incompressible, isotropic model of hyperelasticity of the Neo-Hookean type. Nearly incompressible materials exhibit more pronounced isochoric deformations under large deflections than volumetric ones which hold for many elastomers. The physical reason for the choice of the nearly incompressible approach is the difference of about three orders of magnitude in the numerical values of the bulk and shear moduli. In the kinematic description of nearly incompressible materials the deformation gradient is multiplicatively split into volumetric and isochoric parts as defined by Eq. (14) (cf. Kaliske and Rothert, 1997; Holzapfel, 1996):

$$\mathbf{F} = \mathbf{F}_{vol}\overline{\mathbf{F}} = \left(J^{\frac{1}{3}}\mathbf{1}\right)\left(J^{-\frac{1}{3}}\mathbf{F}\right) \tag{14}$$

Under this assumption, the right Cauchy–Green tensor decomposes as specified in the following equation:

$$\mathbf{C} = \mathbf{C}_{vol}\overline{\mathbf{C}} = \left(J^{\frac{2}{3}}\mathbf{1}\right)\left(J^{-\frac{2}{3}}\mathbf{C}\right) \tag{15}$$

The volume ratio J is defined in the following equation:

$$J = \det\mathbf{F} = \sqrt{\det\mathbf{C}}, \quad \bar{J} = \det\overline{\mathbf{F}} = \sqrt{\det\overline{\mathbf{C}}} = 1 \tag{16}$$

This concept is popular in computational mechanics, because it avoids numerical complications during the solution of finite element structures. A suitable representation of the strain energy function for the nearly compressible isotropic Neo-Hooke material is given by Eq. (17). The scalar p is the hydrostatic pressure which is defined as $p = -(J-1)/d$:

$$\rho_R\psi_{eq} = \rho_R\psi_{vol}(J) + \rho_R\psi_{iso}(\bar{I}_1(\overline{\mathbf{C}})) = p(J-1) + \frac{\mu}{2}(\bar{I}_1(\overline{\mathbf{C}}) - 3) \tag{17}$$

The isochoric part of Eq. (17) depends only on the first invariant of $\bar{I}_1(\overline{\mathbf{C}})$ the isochoric right Cauchy–Green tensor $\overline{\mathbf{C}}$:[2]

$$\bar{I}_1(\overline{\mathbf{C}}) = tr(\overline{\mathbf{C}}) = tr\left(J^{-\frac{2}{3}}\mathbf{C}\right) = J^{-\frac{2}{3}}\mathbf{1}\cdot\mathbf{C} = J^{-\frac{2}{3}}I_1(\mathbf{C}) \tag{18}$$

The final representation of the nearly incompressible Neo-Hookean strain energy function is given by Eq. (19).

$$\psi_{eq}(\mathbf{C}) = \frac{1}{d}\left(\sqrt{\det\mathbf{C}} - 1\right)^2 + \frac{\mu}{2}\left((\det\mathbf{C})^{-\frac{1}{3}}\mathbf{1}\cdot\mathbf{C} - 3\right) \tag{19}$$

On the basis of the strain energy specified in Eq. (19) the Second Piola–Kirchhoff stress in Eq. (21) is derived according to Leibnitz' rule of differentiation, $\partial(\mathbf{1}\cdot\mathbf{C})/\partial\mathbf{C} = \mathbf{1}$,$\partial(\det\mathbf{C})/\partial\,\mathbf{C} = (\det\mathbf{C})\mathbf{C}^{-1}$:

$$\widetilde{\mathbf{T}}_{eq} = 2\frac{\partial\psi_{eq}}{\partial\mathbf{C}} = \widetilde{\mathbf{T}}_{eq(vol)} + \widetilde{\mathbf{T}}_{eq(iso)} \tag{20}$$

$$\begin{aligned}\widetilde{\mathbf{T}}_{eq} = {} & \frac{4}{d}\left(\sqrt{\det\mathbf{C}} - 1\right)\left(\frac{1}{2\sqrt{\det\mathbf{C}}}(\det\mathbf{C})\mathbf{C}^{-1}\right) \\ & + \mu\left(-\frac{1}{3}(\det\mathbf{C})^{-\frac{4}{3}}(\det\mathbf{C})\mathbf{C}^{-1}(\mathbf{1}\cdot\mathbf{C}) + (\det\mathbf{C})^{-\frac{1}{3}}\mathbf{1}\right)\end{aligned}$$

$$\widetilde{\mathbf{T}}_{eq} = \mu J^{-\frac{2}{3}}\mathbf{1} + \left(\frac{2}{d}(J-1)J - \frac{\mu}{3}J^{-\frac{2}{3}}(\mathbf{1}\cdot\mathbf{C})\right)\mathbf{C}^{-1} \tag{21}$$

For the FEM implementation of the constitutive equations, the stress relation is formulated with respect to current configuration. To this end, Eq. (21) is transformed to the current configuration according to the well-known 'push forward' transformation as defined in Eq. (22). As a result, the Cauchy stress tensor of the equilibrium part of the material model (Eq. (23)) is obtained.

$$\mathbf{T}_{eq} = \frac{1}{J}\mathbf{F}\widetilde{\mathbf{T}}_{eq}\mathbf{F}^T \tag{22}$$

In Eq. (23), the tensor $\mathbf{B} = \mathbf{F}\mathbf{F}^T$ is the left Cauchy–Green tensor.

$$\begin{aligned}\mathbf{T}_{eq} &= \mu J^{-\frac{2}{3}}J^{-1}\mathbf{B} + \left(\frac{2}{d}(J-1) - \frac{\mu}{3}J^{-\frac{5}{3}}(\mathbf{1}\cdot\mathbf{B})\right)\mathbf{1} \\ \mathbf{T}_{eq} &= \frac{2}{d}(J-1)\mathbf{1} + \mu J^{-\frac{5}{3}}\left(\mathbf{B} - \frac{1}{3}tr(\mathbf{B})\mathbf{1}\right)\end{aligned} \tag{23}$$

3.6. Overstress response

One possibility of a geometrical nonlinear generalisation of the model for the partial overstresses is given by Eq. (24) under consideration of Eq. (9). The motivation comes from the one-dimensional formulation which is near specified in Eq. (8) (Haupt and Lion, 2002).

[2] $\mathbf{1}$ is the unit tensor, $\mathbf{1}\cdot\mathbf{C} = C_{11} + C_{33} + C_{33}$ is the trace in Cartesian coordinates.

$$\overset{\nabla}{\underset{ovk}{\mathbf{S}}} = 2c_k\mathbf{D} - \frac{H_k(t)}{Z_k}\mathbf{S}_{ovk}, \quad \overset{\nabla}{\underset{ovk}{\mathbf{S}}} = \dot{\mathbf{S}}_{ovk} - \mathbf{L}\mathbf{S}_{ovk} - \mathbf{S}_{ovk}\mathbf{L}^T, \quad \mathbf{D} = \frac{1}{2}(\mathbf{L}+\mathbf{L}^T) \tag{24}$$

The transformation of Eq. (24) to the reference configuration is carried out according to the 'pull back' transformation $\widetilde{\mathbf{T}}_{ovk} = \mathbf{F}^{-1}\mathbf{S}_{ovk}\mathbf{F}^{T-1}$ under the assumption of the relations between the strain rate tensor $\mathbf{D}$ and the derivative of the Piola strain tensor[3] $\mathbf{D} = -\dot{\mathbf{F}}\mathbf{e}\mathbf{F}^T$. The corresponding relation in the form of the partial Second Piola–Kirchhoff overstress reads as follows:

$$\dot{\widetilde{\mathbf{T}}}_{ovk} = -2c_k\dot{\mathbf{e}} - \frac{H_k(t)}{Z_k}\widetilde{\mathbf{T}}_{ovk} \tag{25}$$

In order to obtain equivalent differential equations for internal variables of the strain type the Piola strain tensor is decomposed according to Eq. (26). The new internal variables are denoted as $\mathbf{e}_{ink}$ and can be named as inelastic Piola strains. Considering the one-dimensional formulation specified in Eq. (10), the rate of the Piola strain can be expressed follows:

$$\dot{\mathbf{e}} = \dot{\mathbf{e}}_{el} + \dot{\mathbf{e}}_{ink} = (\dot{\mathbf{e}} - \dot{\mathbf{e}}_{ink}) + \frac{H_k(t)}{Z_k}(\mathbf{e} - \mathbf{e}_{ink}) \tag{26}$$

Inserting Eq. (26) into Eq. (25) we obtain the following expression:

$$\dot{\widetilde{\mathbf{T}}}_{ovk} + \frac{H_k(t)}{Z_k}\widetilde{\mathbf{T}}_{ovk} = -2c_k(\dot{\mathbf{e}} - \dot{\mathbf{e}}_{ink}) - 2c_k\frac{H_k(t)}{Z_k}(\mathbf{e} - \mathbf{e}_{ink}) \tag{27}$$

From Eq. (27) it can be concluded that the partial overstresses of the second Piola–Kirchhoff type must depend on the inelastic Piola strains as given by the following equation:

$$\widetilde{\mathbf{T}}_{ovk} = -2c_k(\mathbf{e} - \mathbf{e}_{ink}) \tag{28}$$

Similar to the equilibrium stress, the formulation of the overstress with respect to the current configuration is needed too. The total overstress with transformed partial overstress is given in Eq. (29). Since rubber is nearly incompressible, i.e. $J \approx 1$, and the weak compressibility is taken into account in the equilibrium stress, it is not necessary to distinguish between the Cauchy overstress $\mathbf{T}_{ov}$ and the weighted Cauchy overstress $\mathbf{S}_{ov} = J\,\mathbf{T}_{ov}$. But in the case of compressible viscoelastic materials this distinction is essential such that Eq. (24) as well as all the consequences have to be reformulated using the isochoric strain rate tensor $\overline{\mathbf{D}} = (\dot{\overline{\mathbf{F}}}\overline{\mathbf{F}}^{-1} + \overline{\mathbf{F}}^{T-1}\dot{\overline{\mathbf{F}}}^T)/2$ (see Eq. (14)).

$$\mathbf{T}_{ov} = \sum_{k=1}^{n}\mathbf{T}_{ovk} = -\sum_{k=1}^{n}\frac{2c_k}{\det\mathbf{F}}\left(\mathbf{F}\mathbf{e}\mathbf{F}^T - \mathbf{F}\mathbf{e}_{ink}\mathbf{F}^T\right) \tag{29}$$

The scalar equations for the scaling functions H_k and the internal variables q_k can be assumed to be similar to those in the one-dimensional formulation (Eqs. (11) and (12)). Only the absolute value of the scalar strain rate in Eq. (12) is replaced by the norm of the symmetric part of the spatial velocity gradient $\|\mathbf{D}\|$.

$$H_k(t) = 1 + d_k q_k(t) \tag{30}$$

$$\dot{q}_k(t) = \frac{1}{\lambda_k}(\|\mathbf{D}\| - q_k) \tag{31}$$

3.7. Norm of strain rate

For the following considerations, the relation between the rate of the Cauchy–Green tensor and the strain rate tensor $\mathbf{D}$ is needed. The corresponding relation, Eq. (32), operates on the current configuration.

$$\mathbf{D} = \frac{1}{2}\mathbf{F}^{T-1}\dot{\mathbf{C}}\mathbf{F}^{-1} \tag{32}$$

[3] The Piola strain tensor is defined as $\mathbf{e} = \frac{1}{2}(\mathbf{C}^{-1} - \mathbf{1})$.

The norm of the strain rate tensor $\mathbf{D}$ is defined by square root of the scalar product with itself.

$$\|\mathbf{D}\|^2 = \mathbf{D}\cdot\mathbf{D} = \sum_{i,j=1}^{3} D_{ij}D_{ij} \tag{33}$$

Using Eqs. (32) and (33), the following result is obtained:

$$\|\mathbf{D}\| = \sqrt{tr(\mathbf{D}\mathbf{D})} = \sqrt{\frac{1}{4}tr\left(\mathbf{F}^{T-1}\dot{\mathbf{C}}\mathbf{F}^{-1}\mathbf{F}^{T-1}\dot{\mathbf{C}}\mathbf{F}^{-1}\right)} = \frac{1}{2}\sqrt{tr\left((\mathbf{C}^{-1}\dot{\mathbf{C}})^2\right)} \tag{34}$$

4. FEM – implementation of the amplitude-dependent model

The material model introduced above was implemented into the commercial FEM code ANSYS in an updated Lagrangean formulation (Crisfield, 1998). The implementation of user-written constitutive models can be realised with the subroutine USERMAT (cf. ANSYS, 2007), which is in the focus of the current section. This subroutine is based on a co-rotational formulation of stresses and strains as formulated by Felippa (2000), Souza (2000), Hughes and Wingets (1980), Seifert et al. (2006), or Simo and Huges (2000). For the implementation of the developed model this approach was not used in the proposed original form. In our procedure, all element quantities are initially computed in the current configuration with respect to the reference coordinate system and then rotated to the current coordinate system. The rotation tensor is computed from the polar decomposition of the deformation gradient. This is a standard approach for applications working with large-strains and rotations which is the case of rubber-like materials. The relations for the equilibrium and overstress tensors of Cauchy type, which are given in Eqs. (35) and (36) at the time step $t_{n+1} = t_n + \Delta t$, are computed using the kinematic relations at the same time. To simplify the nomenclature, $n+1$ is written instead of t_{n+1}. The symbol $|_{(n+1)}$ means that the all quantities on the right-hand side of Eqs. (35) and (36) are evaluated at the time t_{n+1}.

$$\mathbf{T}_{eq}(n+1) = \left[\frac{2}{d}(J-1)\mathbf{1} + \mu J^{-\frac{5}{3}}\left(\mathbf{B} - \frac{1}{3}tr(\mathbf{B})\mathbf{1}\right)\right]\Big|_{(n+1)} \tag{35}$$

$$\mathbf{T}_{ovk}(n+1) = \left[-\frac{2c_k}{J}(\mathbf{F}\mathbf{e}_k\mathbf{F}^T - \mathbf{F}\mathbf{e}_{ink}\mathbf{F}^T)\right]\Big|_{(n+1)} \tag{36}$$

The incremental solution procedure makes both the implementation and the integration of the differential equations for the rates of the state variables (Eq. (31)) and the inelastic Piola strains (Eq. (26)) very comfortable (Hossain et al., 2008; Hossain et al., 2009). Eqs. (37) and (38) are the incremental solutions of Eqs. (26) and (39) with the Euler-Backward algorithm in the recursive form.

$$\mathbf{e}_{ink}(n+1) = \frac{Z_k}{(Z_k + H_k(n+1)\Delta t)}\mathbf{e}_{ink}(n) + \frac{H_k(n+1)\Delta t}{(Z_k + H_k(n+1)\Delta t)}\mathbf{e}(n+1) \tag{37}$$

$$H_k(n+1) = 1 + d_k q_k(n+1) \tag{38}$$

$$q_k(n+1) = \frac{\lambda_k}{\lambda_k + \Delta t}q_k(n) + \frac{\Delta t}{\lambda_k + \Delta t}\|\mathbf{D}(n+1)\| \tag{39}$$

4.1. Norm of strain rate

The rate of the right Cauchy–Green tensor which occurs in the equation for the norm of the strain rate tensor (Eq. (34)) was calculated via the analytical Euler-Backward differentiation formula in

the form of $\dot{\mathbf{C}}(n+1) = (\mathbf{C}(n+1) - \mathbf{C}(n))/\Delta t$. As a result of the calculation, Eq. (40) depends on the tensor $\mathbf{C}^{-1}$ at current time step and on $\mathbf{C}$ at the previous step.

$$\|\mathbf{D}(n+1)\| = \frac{1}{2\Delta t}\sqrt{tr((\mathbf{1} - \mathbf{C}^{-1}(n+1)\mathbf{C}(n))^2)} \tag{40}$$

The expression under the square root of Eq. (40) can be reformulated in order to save computation time:

$$\begin{aligned}&(\mathbf{1} - \mathbf{C}^{-1}(n+1)\mathbf{C}(n))^2\\ &\quad = \mathbf{1} - 2\mathbf{C}^{-1}(n+1)\mathbf{C}(n) + (\mathbf{C}^{-1}(n+1)\mathbf{C}(n))^2\\ &tr((\mathbf{1} - \mathbf{C}^{-1}(n+1)\mathbf{C}(n))^2)\\ &\quad = 3 - 2tr(\mathbf{C}^{-1}(n+1)\mathbf{C}(n)) + tr((\mathbf{C}^{-1}(n+1)\mathbf{C}(n))^2)\end{aligned} \tag{41}$$

Eq. (42) is the final relation to compute the norm of the strain rate tensor which is optimized for the FEM implementation procedure.

$$\|\mathbf{D}(n+1)\| = \frac{1}{2\Delta t}\sqrt{3 - 2tr(\mathbf{C}^{-1}(n+1)\mathbf{C}(n)) + tr((\mathbf{C}^{-1}(n+1)\mathbf{C}(n))^2)} \tag{42}$$

4.2. Tangent operator in the FEM code ANSYS

Implicit incremental solution procedures in the context of finite element analyses require the tangent stiffness matrix. From the principle of virtual work on the element level the linearised tangent stiffness matrix for the updated Lagrangean formulation is derived, see (Crisfield, 1998).

$$\mathbf{K} = \mathbf{K}_M + \mathbf{K}_G = \int_{V_0} \mathbf{B}_l^T \widetilde{\mathbb{C}} \mathbf{B}_l \, dV_0 + \int_{V_0} \mathbf{G}^T \widehat{\mathbf{T}} G \, dV_0 \tag{43}$$

The first term in Eq. (43) $\mathbf{K}_M$ is the material stiffness matrix and second term $\mathbf{K}_G$ the geometrical stiffness matrix. In the context of the FEM implementation of user-defined material models the first term is in the focus. The matrix $\mathbf{B}_l$ connects the changes in the linear strain tensor and the nodal displacement vector. The fourth-order tensor $\widetilde{\mathbb{C}}$ is the material tangent operator which is important for the ANSYS-subroutine USERMAT. Its formulation depends on the kinematic relations of the constitutive model to be implemented. The updated Lagrangean material stiffness matrix, relevant for the FEM code ANSYS, has to be derived from the objective Jaumann rate of the total Kirchhoff stress strain relation in form given in Eq. (44).

$$\mathring{\mathbf{S}} = \widetilde{\mathbb{C}}\mathbf{D} \tag{44}$$

4.3. General formulation of the objective material tangent operator

In the following, the derivation of the objective tangent operator as specified by Eq. (44) on the basis of a model of finite elasticity is presented. To this end, we start with a stress–strain relation in the reference configuration and calculate its time rate (Eq. (45)). In the case of linear elasticity, the tangent operator equals the fourth-order elastic modulus tensor. But in more general cases, the tangent operator with respect to the reference configuration is the partial derivative of the second Piola–Kirchhoff stress (Eq. (46)) with regard to the right Cauchy–Green tensor.

$$\begin{aligned}&\widetilde{\mathbf{T}} = \widetilde{\mathbf{T}}(\mathbf{C})\\ &\dot{\widetilde{\mathbf{T}}} = \frac{\partial \widetilde{\mathbf{T}}}{\partial \mathbf{C}}\dot{\mathbf{C}} = 2\frac{\partial \widetilde{\mathbf{T}}}{\partial \mathbf{C}}\dot{\mathbf{E}}\end{aligned} \tag{45}$$

$$\mathbb{C}_R = 2\frac{\partial \widetilde{\mathbf{T}}}{\partial \mathbf{C}} \tag{46}$$

To transform Eq. (45) to the current configuration, Eq. (32) in combination with $\overset{\nabla}{\mathbf{S}} = \mathbf{F}\dot{\widetilde{\mathbf{T}}}\mathbf{F}^T$ were used; the left-hand side of Eq. (47) is the Oldroyd rate of the Kirchhoff stress. Using the linear tensor transformation $\mathbf{B}^T\mathbf{C}\mathbf{A} = (\mathbf{A}\otimes\mathbf{B})^{T_{14}}\mathbf{C}$ as applied, for example, by Hartman (2003) or Ehlers (1999), Eq. (48) is the reformulation of Eq. (47). In this way, the strain rate tensor can be separated. The factor of the tensor $\mathbf{D}$ in Eq. (48) is the fourth-order material tangent operator in the spatial configuration, see also in Hartman and Haupt (1999).

$$\overset{\nabla}{\mathbf{S}} = \mathbf{F}\mathbb{C}_R\mathbf{F}^T\mathbf{D}\mathbf{F}\mathbf{F}^T \tag{47}$$

$$\overset{\nabla}{\mathbf{S}} = \left[\mathbf{F}^T\otimes\mathbf{F}^T\right]^{T_{14}}\mathbb{C}_R[\mathbf{F}\otimes\mathbf{F}]^{T_{14}}\mathbf{D} \tag{48}$$

Considering the definition of the contravariant Oldroyd stress rate (Eq. (49)), the time rate of the Kirchhoff stress can be derived. Inserting Eq. (48) in combination with the decomposition of the velocity gradient into Eqs. (49) and (50) is obtained. For the velocity gradient and its symmetric and antisymmetric parts the following relations are valid: $\mathbf{L} = \mathbf{D} + \mathbf{W},\ \mathbf{D} = \mathbf{D}^T, \mathbf{W} = -\mathbf{W}^T$

$$\overset{\nabla}{\mathbf{S}} = \dot{\mathbf{S}} - \mathbf{L}\mathbf{S} - \mathbf{S}\mathbf{L}^T \tag{49}$$

$$\begin{aligned}\dot{\mathbf{S}} = &\left[\left[\mathbf{F}^T\otimes\mathbf{F}^T\right]^{T_{14}}\mathbb{C}_R[\mathbf{F}\otimes\mathbf{F}]^{T_{14}} + [\mathbf{S}\otimes\mathbf{1}]^{T_{14}} + [\mathbf{1}\otimes\mathbf{S}]^{T_{14}}\right]\mathbf{D} + \mathbf{W}\mathbf{S}\\ &- \mathbf{S}\mathbf{W}\end{aligned} \tag{50}$$

As a consequence of these calculations, Eq. (51) is the required relation between the Jaumann rate of the Kirchhoff stress and the strain rate tensor. The factor of the strain rate $\mathbf{D}$ is a tensor of the fourth order and can be interpreted as the objective material tangent operator.

$$\begin{aligned}&\mathring{\mathbf{S}} = \dot{\mathbf{S}} + \mathbf{S}\mathbf{W} - \mathbf{W}\mathbf{S}\\ &\mathring{\mathbf{S}} = \left[\left[\mathbf{F}^T\otimes\mathbf{F}^T\right]^{T_{14}}\mathbb{C}_R[\mathbf{F}\otimes\mathbf{F}]^{T_{14}} + [\mathbf{S}\otimes\mathbf{1}]^{T_{14}} + [\mathbf{1}\otimes\mathbf{S}]^{T_{14}}\right]\mathbf{D} = \widetilde{\mathbb{C}}\mathbf{D}\end{aligned} \tag{51}$$

For the FEM implementation of the model in the subroutine USERMAT the tangent operator at the time step $n+1$ containing the Cauchy stress (Eq. (52)) is required. This can be achieved by setting $\mathbf{S} = (\det\mathbf{F})\mathbf{T}$ in Eq. (51) as follows:

$$\begin{aligned}\widetilde{\mathbb{C}}(n+1) = &\left[\left[\mathbf{F}^T\otimes\mathbf{F}^T\right]^{T_{14}}\mathbb{C}_R[\mathbf{F}\otimes\mathbf{F}]^{T_{14}}\right.\\ &\left.+ \det\mathbf{F}\left([\mathbf{T}\otimes\mathbf{1}]^{T_{14}} + [\mathbf{1}\otimes\mathbf{T}]^{T_{14}}\right)\right]\Big|_{n+1}\end{aligned} \tag{52}$$

The additive decomposition of the stress tensor in Eq. (13) leads to a corresponding decomposition of the material stiffness operator into the sum of equilibrium and overstress parts (Eq. (53)).

$$\widetilde{\mathbb{C}} = \widetilde{\mathbb{C}}_{eq} + \sum_{k=1}^{n}\widetilde{\mathbb{C}}_{ovk} \tag{53}$$

4.4. Overstress part of material stiffness matrix

The partial overstress as specified in Eq. (28) can be formulated as function of the right Cauchy–Green tensor (see Eq. (54)). From the mathematical point of view, the partial overstress is a tensor function multiplied with a constant material parameter.

$$\widetilde{\mathbf{T}}_{ovk} = -c_k\left(\mathbf{C}^{-1} - \mathbf{C}_{ink}^{-1}\right) \tag{54}$$

Applying Eqs. (46)–(54), the following expression is obtained:

$$\begin{aligned}\mathbb{C}_{Rovk} &= 2\frac{\partial \widetilde{\mathbf{T}}_{ovk}}{\partial \mathbf{C}}\\ &= 2\left[\left(\mathbf{C}^{-1} - \mathbf{C}_{ink}^{-1}\right)\otimes\frac{\partial(-c_k)}{\partial\mathbf{C}} - c_k\frac{\partial\left(\mathbf{C}^{-1} - \mathbf{C}_{ink}^{-1}\right)}{\partial\mathbf{C}}\right]\end{aligned} \tag{55}$$

For the partial derivatives in Eq. (55), the following relations hold:

$$\frac{\partial \mathbf{C}^{-1}}{\partial \mathbf{C}} = -(\mathbf{C}^{-1}\otimes\mathbf{C}^{T-1})^{T_{23}} = -(\mathbf{C}^{-1}\otimes\mathbf{C}^{-1})^{T_{23}} \tag{56}$$
$$\frac{\partial(-c_k)}{\partial \mathbf{C}} = 0$$

Finally, the material tangent operator of the partial overstress in the reference configuration is obtained as:

$$\mathbb{C}_{ov k} = 2\frac{\partial \widetilde{\mathbf{T}}_{ov k}}{\partial \mathbf{C}} = 2c_k(\mathbf{C}^{-1}\otimes\mathbf{C}^{-1})^{T_{23}} \tag{57}$$

Taking Eq. (52) into account and computing the sum of the partial overstresses produced from all Maxwell elements, the final form of the objective tangent operator of the overstress is obtained as:

$$\widetilde{\mathbb{C}}_{ov}(n+1) = \left[\sum_{k=1}^{n}\left\{2c_k\left[\mathbf{F}^T\otimes\mathbf{F}^T\right]^{T_{14}}\left(\mathbf{C}^{-1}\otimes\mathbf{C}^{-1}\right)^{T_{23}}[\mathbf{F}\otimes\mathbf{F}]^{T_{14}} + \det\mathbf{F}\left([\mathbf{T}_k\otimes\mathbf{1}]^{T_{14}} + [\mathbf{1}\otimes\mathbf{T}_k]^{T_{14}}\right)\right\}\right]\Big|_{n+1} \tag{58}$$

4.5. Equilibrium part of material stiffness matrix

One way to formulate the objective tangent operator is based on Eq. (52) as derived in Section 4.3. Another method is the direct calculation of the Jaumann derivative from the stress–strain relation and the separation of the strain rate tensor **D**, which is done in this section. As a first step, we formulate the hyperelastic relation of the equilibrium stress, Eq. (23), in the form of the Kirchhoff stress using $\mathbf{S} = J\,\mathbf{T}$.

$$\mathbf{S}_{eq} = \frac{2J}{d}(J-1)\mathbf{1} + \mu J^{-\frac{2}{3}}\left(\mathbf{B} - \frac{1}{3}tr(\mathbf{B})\mathbf{1}\right) \tag{59}$$

Then, the time rate of the Kirchhoff stress is calculated.

$$\dot{\mathbf{S}}_{eq} = \left(\frac{2\dot{J}}{d}(J-1) + \frac{2J\dot{J}}{d}\right)\mathbf{1} - \frac{2}{3}\mu J^{-\frac{5}{3}}\dot{J}\left(\mathbf{B} - \frac{1}{3}(\mathbf{1}\cdot\mathbf{B})\mathbf{1}\right) + \mu J^{-\frac{2}{3}}\dot{J}\left(\dot{\mathbf{B}} - \frac{1}{3}(\mathbf{1}\cdot\dot{\mathbf{B}})\mathbf{1}\right) \tag{60}$$

On the basis of the velocity gradient $\mathbf{L} = \dot{\mathbf{F}}\mathbf{F}^{-1}$ and its additive decomposition, the rate of the left Cauchy–Green tensor is reformulated.

$$\dot{\mathbf{B}} = (\mathbf{F}\mathbf{F}^T)^{\cdot} = \dot{\mathbf{F}}\mathbf{F}^T + \mathbf{F}\dot{\mathbf{F}}^T = \mathbf{L}\mathbf{B} + \mathbf{B}\mathbf{L}^T = (\mathbf{D}+\mathbf{W})\mathbf{B} + \mathbf{B}(\mathbf{D}-\mathbf{W}) = \mathbf{D}\mathbf{B} + \mathbf{B}\mathbf{D} + \mathbf{W}\mathbf{B} - \mathbf{B}\mathbf{W} \tag{61}$$

The relation for the material time derivative of the scalar field $J = \det\mathbf{F}$ is given in Eq. (62). The fact that the trace of antisymmetric tensors is zero was also taken into account.

$$\dot{J} = J\,tr(\mathbf{L}) = J\,\mathbf{D}\cdot\mathbf{1} = 0 \tag{62}$$

Inserting Eqs. (61) and (62) into Eq. (60) leads to Eq. (63) which is used to compute the Jaumann rate of the Kirchhoff stress.

$$\dot{\mathbf{S}}_{eq} = \left(\frac{4J-2}{d}\mathbf{1} - \frac{2}{3}\mu J^{-\frac{5}{3}}\left(\mathbf{B} - \frac{1}{3}(\mathbf{1}\cdot\mathbf{B})\mathbf{1}\right)\right)J\mathbf{D}\cdot\mathbf{1} + \mu J^{-\frac{2}{3}}\left(\mathbf{D}\mathbf{B}+\mathbf{B}\mathbf{D}+\mathbf{W}\mathbf{B}-\mathbf{B}\mathbf{W} - \frac{1}{3}([\mathbf{D}\mathbf{B}+\mathbf{B}\mathbf{D}+\mathbf{W}\mathbf{B}-\mathbf{B}\mathbf{W}]\cdot\mathbf{1})\mathbf{1}\right) \tag{63}$$

Eq. (63) can be simplified using the following property of the trace operator:

$$(\mathbf{W}\mathbf{B}-\mathbf{B}\mathbf{W})\cdot\mathbf{1} = tr(\mathbf{W}\mathbf{B}-\mathbf{B}\mathbf{W}) = tr(\mathbf{W}\mathbf{B}) - tr(\mathbf{W}\mathbf{B}) = 0 \tag{64}$$

In the case of a Neo-Hookean model for the equilibrium stress (see Eq. (59)), the last two terms of the Jaumann rate (see Eq. (66)) can be reduced:

$$\mathbf{S}_{eq}\mathbf{W} - \mathbf{W}\mathbf{S}_{eq} = \mu J^{-\frac{2}{3}}(\mathbf{B}\mathbf{W} - \mathbf{W}\mathbf{B}) \tag{65}$$

According Eqs. (63)–(65) the Jaumann rate of the Kirchhoff stress reads as follows:

$$\overset{\circ}{\mathbf{S}}_{eq} = \dot{\mathbf{S}}_{eq} + \mathbf{S}_{eq}\mathbf{W} - \mathbf{W}\mathbf{S}_{eq}$$
$$\overset{\circ}{\mathbf{S}}_{eq} = \left(\frac{4J-2}{d}\mathbf{1} - \frac{2}{3}\mu J^{-\frac{5}{3}}\left(\mathbf{B} - \frac{1}{3}(\mathbf{1}\cdot\mathbf{B})\mathbf{1}\right)\right)J\mathbf{D}\cdot\mathbf{1} + \mu J^{-\frac{2}{3}}\left(\mathbf{D}\mathbf{B}+\mathbf{B}\mathbf{D} - \frac{1}{3}([\mathbf{D}\mathbf{B}+\mathbf{B}\mathbf{D}]\cdot\mathbf{1})\mathbf{1}\right) \tag{66}$$

In order to separate the strain rate tensor **D** from the other terms, the last terms on the right-hand side of Eq. (66) are reformulated as given in Eq. (67):

$$([\mathbf{D}\mathbf{B}+\mathbf{B}\mathbf{D}]\cdot\mathbf{1})\mathbf{1} = (tr(\mathbf{D}\mathbf{B}+\mathbf{B}\mathbf{D}))\mathbf{1} = 2tr(\mathbf{D}\mathbf{B})\mathbf{1} = 2\mathbf{1}(\mathbf{B}\cdot\mathbf{D}) = [\mathbf{1}\otimes\mathbf{B}]\mathbf{D} \tag{67}$$
$$\mathbf{D}\mathbf{B}+\mathbf{B}\mathbf{D} = \mathbf{1}\mathbf{D}\mathbf{B} + \mathbf{B}\mathbf{D}\mathbf{1} = \left[\mathbf{B}\otimes\mathbf{1}^T\right]^{T_{14}}\mathbf{D} + \left[\mathbf{1}\otimes\mathbf{B}^T\right]^{T_{14}}\mathbf{D}$$

Using the relation $\mathbf{B}^T\mathbf{C}\mathbf{A} = (\mathbf{A}\otimes\mathbf{B})^{T_{14}}\mathbf{C}$, Eq. (66) can be rewritten such that the strain rate tensor is separated:

$$\overset{\circ}{\mathbf{S}}_{eq} = \frac{J(4J-2)}{d}[\mathbf{1}\otimes\mathbf{1}]\mathbf{D} - \frac{2}{3}\mu J^{-\frac{2}{3}}[\mathbf{1}\otimes\mathbf{B}]\mathbf{D} + \frac{2}{9}\mu J^{-\frac{2}{3}}tr(\mathbf{B})[\mathbf{1}\otimes\mathbf{1}]\mathbf{D} + \mu J^{-\frac{2}{3}}\left([\mathbf{B}\otimes\mathbf{1}]^{T_{14}} + [\mathbf{1}\otimes\mathbf{B}]^{T_{14}}\right)\mathbf{D} - \frac{2}{3}\mu J^{-\frac{2}{3}}[\mathbf{1}\otimes\mathbf{B}]\mathbf{D} \tag{68}$$

In Eq. (69), the fourth-order tensor from Eq. (68) is separated. It is the equilibrium part of the tangent operator. It can be shown that Eq. (69) is equal to the formulation proposed by Bonet and Wood (1997).

$$\widetilde{\mathbb{C}}_{eq} = \left[\mu J^{-\frac{2}{3}}([\mathbf{B}\otimes\mathbf{1}]^{T_{14}} + [\mathbf{1}\otimes\mathbf{B}]^{T_{14}}) - \frac{2}{3}\mu J^{-\frac{2}{3}}([\mathbf{1}\otimes\mathbf{B}] + [\mathbf{1}\otimes\mathbf{B}]) + \left(\frac{J(4J-2)}{d} + \frac{2}{9}\mu J^{-\frac{2}{3}}tr(\mathbf{B})\right)[\mathbf{1}\otimes\mathbf{1}]\right]\Big|_{n+1} \tag{69}$$

The total objective tangent operator which is needed for the ANSYS implementation of the developed constitutive model is given by the sum of Eqs. (58) and (59) as given in Eq. (53).

4.6. Primary framework of the stress update in USERMAT

The kinematic formulation of the ANSYS-subroutine USERMAT (ANSYS, 2007) is based on a co-rotational formulation. This approach is based on an old idea: the separation of rigid body and purely deformational motions in continuum mechanics (Veubeke, 1976). This means that the stress is computed on the basis of already rotated quantities. The specification of co-rotational frames can be found, for example, in Felippa (2000), Souza (2000), Hughes and Wingets (1980) or Seifert and Maier (2008) and Simo and Hughes (2000). This approach consists of two steps for the stress update. During the time increment Δt all kinematic relations working on the element level are rotated and then updated. The first step is the rotation of all quantities to the current spatial coordinate system. The rotation of the Cauchy stress tensor $\mathbf{T}_R(n)$, accepted in the previous time step, to the current coordinate system is given by Eq. (70). $\Delta\mathbf{R}$ is the incremental rotation tensor between the two time steps.

$$\mathbf{T}_C(n) = \Delta\mathbf{R}\mathbf{T}_R(n)\Delta\mathbf{R}^T \tag{70}$$

The computation of $\Delta\mathbf{R}$ is based on the incremental displacement gradient $\Delta\mathbf{H}$ which is related to the incremental deformation gradient $\Delta\mathbf{F}$ between the two steps, i.e. $\mathbf{F}(n+1) = \Delta\mathbf{F}\mathbf{F}(n)$ with $\Delta\mathbf{F} = \mathbf{1} + \Delta\mathbf{H}$ and $\|\Delta\mathbf{H}\| \ll 1$. Under these assumptions, the approximations $(\Delta\mathbf{F})^{-1} = \mathbf{1} - \Delta\mathbf{H}$, $\Delta\mathbf{B} = \mathbf{1} + \Delta\mathbf{H} + \Delta\mathbf{H}^T$, $\Delta\mathbf{V} = \mathbf{1} + (\Delta\mathbf{H} + \Delta\mathbf{H}^T)/2$,

$\Delta\mathbf{L} = \Delta\dot{\mathbf{F}}(\Delta\mathbf{F})^{-1} = \Delta\dot{\mathbf{H}}$, $\Delta\mathbf{D} = (\Delta\dot{\mathbf{H}} + \Delta\dot{\mathbf{H}}^T)/2$ as well as $\Delta\mathbf{W} = (\Delta\dot{\mathbf{H}} - \Delta\dot{\mathbf{H}}^T)/2$ hold. On the basis of the polar decomposition of the incremental deformation gradient $\Delta\mathbf{F} = \Delta\mathbf{V}\Delta\mathbf{R}$ the incremental rotation tensor $\Delta\mathbf{R} = \Delta\mathbf{V}^{-1}\Delta\mathbf{F}$ is computed as described, for example, by Haupt (2000) or Crisfield (1997):

$$\Delta\mathbf{R} = \left(\mathbf{1} - \frac{1}{2}\left(\Delta\mathbf{H} + \Delta\mathbf{H}^T\right)\right)(\mathbf{1} + \Delta\mathbf{H}) = \mathbf{1} + \frac{1}{2}\left(\Delta\mathbf{H} - \Delta\mathbf{H}^T\right) \tag{71}$$

Since $\|\Delta\mathbf{H}\| \ll 1$ is assumed, the quadratic term has been neglected in Eq. (71). The approximation of the incremental spin tensor $\Delta\mathbf{W} = (\Delta\dot{\mathbf{H}} - \Delta\dot{\mathbf{H}}^T)/2$ leads to the following approximation of the incremental rotation tensor:

$$\Delta\mathbf{R} = \mathbf{1} + \Delta\mathbf{W}\Delta t \tag{72}$$

Inserting Eq. (72) into Eq. (70) leads to Eq. (73) for the rotated stress tensor $\mathbf{T}_C(n)$ at the previous time step in the current coordinate system.

$$\begin{aligned}\mathbf{T}_C(n) = \mathbf{T}_R(n) &+ \mathbf{T}_R(n)(\Delta\mathbf{W})^T\Delta t + \Delta t(\Delta\mathbf{W})\mathbf{T}_R(n) \\ &+ (\Delta\mathbf{W})\mathbf{T}_R(n)(\Delta\mathbf{W})^T\Delta t^2\end{aligned} \tag{73}$$

Since the quadratic term is small it is neglected in the following. The rotation of the entities is an internal process which is running automatically in the FE-software. In the case of small strains, the USERMAT-subroutine gives back the Henckys' strain tensor and the strain increment in the corresponding coordinate system. Thus, the user has only to formulate and to code the equations for the stress increment. This makes the implementation fairly easy.

$$\Delta\mathbf{T} = \widetilde{\mathbb{C}}\Delta\mathbf{e} \quad \text{with} \quad \Delta\mathbf{e} = \Delta\mathbf{D}\Delta t \tag{74}$$

The second step is the calculation of the stress increment on the basis of the tangent operator and the appropriate, rotation-free, strain increment. The updated total stress is the sum of the stress increment and the rotated stress from the previous time step.

$$\mathbf{T}_C(n+1) = \mathbf{T}_C(n) + \Delta\mathbf{T} \tag{75}$$

Inserting Eqs. (73) and (74) into Eqs. (75) and (76) is obtained. It allows interpreting the tangent operator $\widetilde{\mathbb{C}}$ with regard to the Jaumann derivative calculated with the incremental spin tensor.

$$\begin{aligned}\mathbf{T}_C(n+1) &= \mathbf{T}_R(n) + \left(\mathbf{T}_R(n)(\Delta\mathbf{W})^T + (\Delta\mathbf{W})\mathbf{T}_R(n) + \widetilde{\mathbb{C}}\Delta\mathbf{D}\right)\Delta t \\ &= \mathbf{T}_R(n) + \dot{\mathbf{T}}_R(n)\Delta t\end{aligned} \tag{76}$$

The property $\Delta\mathbf{W} = -\Delta\mathbf{W}^T$ of skew-symmetric tensors was taken into account. In Section 4.2 in Eq. (44), the Jaumann derivative of the Kirchhoff stress tensor was calculated.

$$\overset{\circ}{\mathbf{T}}_R = \dot{\mathbf{T}}_R(n) - \Delta\mathbf{W}\,\mathbf{T}_R(n) + \mathbf{T}_R(n)\Delta\mathbf{W} = \widetilde{\mathbb{C}}\Delta\mathbf{D} \tag{77}$$

4.7. Updating algorithm for amplitude-dependent viscoelasticity (USERMAT)

To implement materials models for large deformations with complex evolution equations into FE-codes, the co-rotational formulation as described previously is too complicated. Thus in the following, another algorithm is applied. In this approach, the stress update, the tangent operator and the internal variables are calculated in the coordinate system of the reference configuration. Then, the tangent operator and the stress are rotated to the current coordinate system. Schematically is the update process depicted on Fig. 13.

The new implementation framework is based on the deformation gradient. It is provided by the USERMAT-subroutine in the material coordinate system of the reference configuration $(\mathbf{E}_1, \mathbf{E}_2, \mathbf{E}_3)$ and given at the times t and $t + \Delta t$. The main difference to the standard implementation is that all kinematic variables, the tangent and the stress are at first computed in the material coordinate system of the reference configuration and then rotated to the current frame. The material point $\mathbf{X}$ is described in the material coordinate system of the reference configuration. At the time t or the step n, it is at a certain location in the "previous" current configuration and at the time $t + \Delta t$ this point is in the "new" current state and can be parameterized in the new coordinate system $(\mathbf{e}_1, \mathbf{e}_2, \mathbf{e}_3)$. The rotation tensor $\mathbf{R}$ between these two systems is computed from the polar decomposition of the deformation gradient. Eq. (35) determining the equilibrium stress and Eq. (36) the overstress are used in the iterative solution procedure to compute the stress increments in the material coordinate system. Accordingly, the sum in Eq. (13) is used to compute the total stress increment. It is rotated to the current coordinate system according to Eq. (78).

$$\begin{aligned}\Delta\mathbf{T}_C &= \mathbf{R}\Delta\mathbf{T}_R\mathbf{R}^T = (\mathbf{R}^T \otimes \mathbf{R}^T)^{T_{14}}\Delta\mathbf{T}_R = (\mathbf{R}\otimes\mathbf{R})^{T_{23}}\Delta\mathbf{T}_R \\ &= \overset{4}{\mathbf{Q}}\Delta\mathbf{T}_R \triangleq \mathbf{Q}\Delta\mathbf{T}_R\end{aligned} \tag{78}$$

The matrix $\mathbf{Q}$ is the reduced 6×6 rotation matrix of second-order belonging to the rotation tensor of the fourth-order $\overset{4}{\mathbf{Q}}$. This reduction is feasible because the stress tensor is symmetric and a maximum of 36 elements is needed to formulate the most general linear transformation.

$$\begin{aligned}\Delta\widetilde{\mathbb{C}}_C &= \overset{4}{\mathbf{Q}}\Delta\widetilde{\mathbb{C}}_R\overset{4}{\mathbf{Q}}^T = (\mathbf{R}\otimes\mathbf{R})^{T_{23}}\Delta\widetilde{\mathbb{C}}_R\left((\mathbf{R}\otimes\mathbf{R})^{T_{23}}\right)^T \\ &= (\mathbf{R}\otimes\mathbf{R})^{T_{23}}\Delta\widetilde{\mathbb{C}}_R(\mathbf{R}^T\otimes\mathbf{R}^T)^{T_{23}}\Delta\widetilde{\mathbb{C}}_R \triangleq \mathbf{Q}\Delta\widetilde{\mathbb{C}}_R\mathbf{Q}^T\end{aligned} \tag{79}$$

Eq. (53) and its elements as specified in Eqs. (58) and (69) define the consistent tangent operator in the implementation framework. Similar to the stress tensor, the tangent operator is also rotated to

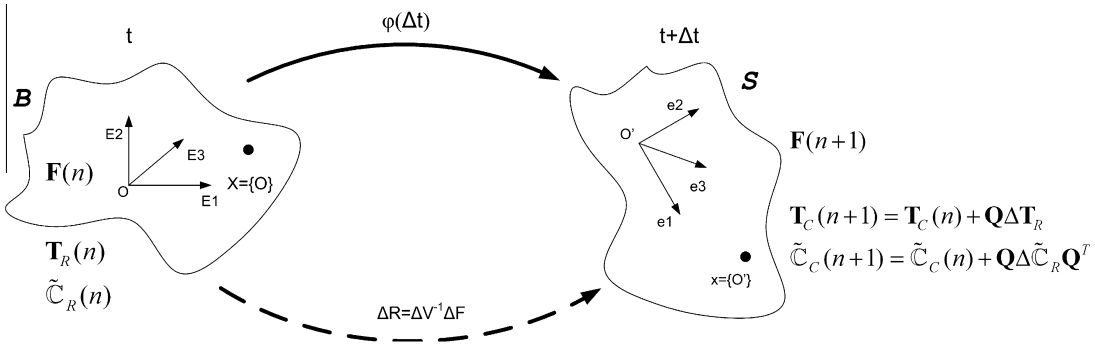

Fig. 13. Incremental update of the stress and stiffness tensors. ***B*** is the material configuration at the time t with the reference frame and ***S*** the material configuration at the time $t + \Delta t$ with the current frame.

Table 1
Workflow of implementation based on deformation gradient.

1	Given from the database	$\mathbf{F}(n)$, $\mathbf{F}(n+1)$
2	Compute kinematic measures in reference c. sys	$\mathbf{C}(n+1), \mathbf{C}^{-1}(n+1), \mathbf{C}(n), \mathbf{C}^{-1}(n)$, $\det \mathbf{F}(n+1), \mathbf{B}(n+1), \mathbf{e}(n+1)$
3	Compute norm of strain rate	$\|\mathbf{D}(n+1)\|$
4	Update state variable q_k and inelastic strain $\mathbf{e}_{ink}$ at each Maxwell element from previous substep	$q_k(n) = ustate\,v$ $\mathbf{e}_{ink}(n) = ustate\,v$
5	Compute new state variable	$q_k(n+1)\,\mathbf{e}_{ink}(n+1)$ and $H_k(n+1)$
6	Compute incremental rotation tensor	$\mathbf{R}(n+1) = \mathbf{V}^{-1}\mathbf{F}\|_{n+1}$
7	Compute incremental stress	$\Delta\mathbf{T}_R(n+1) = \left[\Delta\mathbf{T}_{eqR} + \sum_{k=1}^{n} \Delta\mathbf{T}_{ovkR}\right]\Big\|_{n+1}$
8	Update and rotate total stress	$\mathbf{T}_C(n+1) = \mathbf{T}_C(n) + \mathbf{Q}\,\Delta\mathbf{T}_R$
9	Compute incremental tangent operator	$\Delta\widetilde{\mathbb{C}}(n+1) = \left[\Delta\widetilde{\mathbb{C}}_{eq} + \sum_{k=1}^{n} \Delta\widetilde{\mathbb{C}}_{ovk}\right]\Big\|_{n+1}$
10	Update and rotate tangent operator	$\widetilde{\mathbb{C}}_C(n+1) = \widetilde{\mathbb{C}}_C(n) + \mathbf{Q}\Delta\widetilde{\mathbb{C}}_R\mathbf{Q}^T$
11	Save internal variable from converged substep	$ustate\,v = q_k(n+1)$ $ustate\,v = \mathbf{e}_{ink}(n+1)$

the correct coordinate system according to Eq. (79). The scalar internal variables q_k (Eq. (39)) and the inelastic strain tensors $\mathbf{e}_{ink}$ (Eq. (37)) are declared as state variables and are updated after each converged substep. The summary of the computation procedure during the iteration is given in Table 1.

5. Material parameter identification

The constitutive equations contain a set of parameters representing the material properties which must be determined by experiments. The formulation of the constitutive model is possible in both the time and the frequency domain. The possibility to identify the material parameters on the basis of the stress-time signals or dynamic modulus curves is provided. The identification process based on the dynamic modulus is faster and the identified material constants are valid in wider ranges of frequencies and amplitudes.

5.1. Material model in the frequency domain

The topic of this section is the formulation of the constitutive model presented in Section 3 in the frequency domain. Under the assumption of harmonic strain-controlled excitations with sufficient small amplitudes and a superimposed static preload, all variables oscillate with the same angular frequency ω (higher frequency contributions are assumed to be small). In addition, it is assumed that the internal state variables q_k or the functions $H_k(t)$ which are determined by Eqs. (30) and (31) are nearly constant during a period of oscillation of the dynamic strain. This is the case, when the time constants λ_k in Eq. (31) are large in comparison with the period of oscillation of the dynamic strain excitation, see, e.g. Lion (2004). Under these assumptions, the method as described in Lion et al. (2009) can be applied in order to linearize the constitutive model. The result of this process is a complex dynamic modulus tensor of the fourth order:[4]

$$\overset{4}{\mathbf{G}}_0(\omega) = 4(\mathbf{F}_0 \otimes \mathbf{F}_0)^{T_{23}} \frac{\partial^2 \psi_{eq}}{\partial \mathbf{C}^2}\bigg|_{\mathbf{C}_0} \left(\mathbf{F}_0^T \otimes \mathbf{F}_0^T\right)^{T_{23}} + \sum_{k=1}^{n} \frac{2i\omega c_k Z_k}{1 + d_k q_k(t) + i\omega Z_k} \left(\overset{4}{\mathbf{1}} - \frac{1}{3}\mathbf{1}\otimes\mathbf{1}\right) \tag{80}$$

It depends on the frequency ω of the dynamic strain excitation, the deformation gradient $\mathbf{F}_0$ of the static preload and the internal variables q_k which are introduced to represent the amplitude dependence and are modelled by Eq. (31). The stress tensor belonging to the statically-preloaded configuration is given by the following expression:

$$\mathbf{T}_0 = 2\mathbf{F}_0 \frac{\partial \psi_{eq}}{\partial \mathbf{C}}\bigg|_{\mathbf{C}_0} \mathbf{F}_0^T + \overset{4}{\mathbf{G}}_0(\omega)\Delta\mathbf{E}_{lin} e^{i\omega t} \tag{81}$$

The first term in Eq. (81) is the so-called static stress which is not of interest for the following argumentation. The second term describes the oscillating part of the stress and is determined by the dynamic modulus tensor. In the case of incompressible material behaviour and dynamic tension/compression loadings, the dynamic strain amplitude tensor $\Delta\mathbf{E}_{lin}$ is deviatoric and reads as follows:

$$\Delta\mathbf{E}_{lin} = \Delta\varepsilon\left(\mathbf{e}_1 \otimes \mathbf{e}_1 - \frac{1}{2}(\mathbf{e}_2 \otimes \mathbf{e}_2 + \mathbf{e}_3 \otimes \mathbf{e}_3)\right) \tag{82}$$

Evaluating the right-hand side of Eq. (81) under consideration of Eqs. (80) and (82) and assuming the static preload to be small, i.e. $\mathbf{F}_0 \approx \mathbf{1}$, the uniaxial dynamic modulus is given by the following scalar expression:

$$E^*(\omega) = \frac{4}{\lambda_0}\frac{\partial^2 \psi_{eq}}{\partial \mathbf{C}^2}\bigg|_{\lambda_0} + \frac{2}{3\lambda_0}\sum_{k=1}^{n} \frac{2i\omega c_k Z_k}{1 + d_k q_k(t) + i\omega Z_k} \tag{83}$$

In the case of the applied Neo-Hooke model, the influence of the static preload to the local slope of the equilibrium stress–strain curve is small up to about 30% static strain. In Fig. 5 it can be seen, that the dynamic modulus is nearly independent on the static strain if the static preloads are smaller than 50%. The first part of Eq. (83) can be interpreted as the frequency independent static stiffness of the equilibrium stress–strain curve. Splitting the complex modulus Eq. (83) into real and imaginary parts leads to the expressions for the storage and the loss modulus:

$$E'(\omega, t) = \frac{4}{\lambda_0}\frac{\partial^2 \psi_{eq}}{\partial \mathbf{C}^2}\bigg|_{\lambda_0} + \frac{2}{3\lambda_0}\sum_{k=1}^{n} \frac{2Z_k \eta_k (Z_k\omega)^2}{(1 + d_k q_k(t))^2 + (Z_k\omega)^2} \tag{84}$$

$$E''(\omega, t) = \frac{2}{3\lambda_0}\sum_{k=1}^{n} \frac{2\eta_k \omega (1 + d_k q_k(t))}{(1 + d_k q_k(t))^2 + (Z_k\omega)^2} \tag{85}$$

For time-dependent transient processes, for example harmonic strain-controlled excitations with stepwise changing amplitudes, the numerical solution of the differential equation for the internal variables, Eq. (31), must be calculated and inserted into Eqs. (84) and (85). But, if the transient behaviour after an amplitude change (e.g. in Fig. 1) is not of interest, the stationary solution of Eq. (31) can be taken into the account as published, e.g. in Rendek and Lion (2009a,b). It is a linear function of the dynamic strain amplitude; see also in Lion (2004).

Due to the structure of the model, the identification process is based on two steps. At first, sufficient small strain amplitude of about 0.1% is applied such that the dynamic moduli are time- and amplitude-independent. In this case, we have $H_k(t) \equiv 1$ and $q_k(t) \equiv 0$. Thus, the material parameters c_k, η_k and μ can be determined by means of the frequency sweep in Fig. 14-L. In the second step, the constants d_k and λ_k in Eqs. (30) and (31) describing the amplitude dependence are identified on the basis of the multi-step experiment at 10 Hz (Fig. 14-R). To identify the time- and amplitude-dependent modulus it is necessary to solve the evolution equations, Eq. (31), for the variables q_k. To reduce the extremely long simulation times for the parameter identification of the time-dependent behaviour, the time-axis of the test shown in Fig. 14-R was compressed by a factor of 180. Then, the hold times of 2700 s from the DMA test (Fig. 9) at constant amplitudes were reduced to 15 s. The advantage of this scaling is the reduction of the computation times, particularly with regard to long-term simulations in the time domain. In both steps, the parameter identifi-

[4] The constant $i = \sqrt{-1}$ is the complex unit.

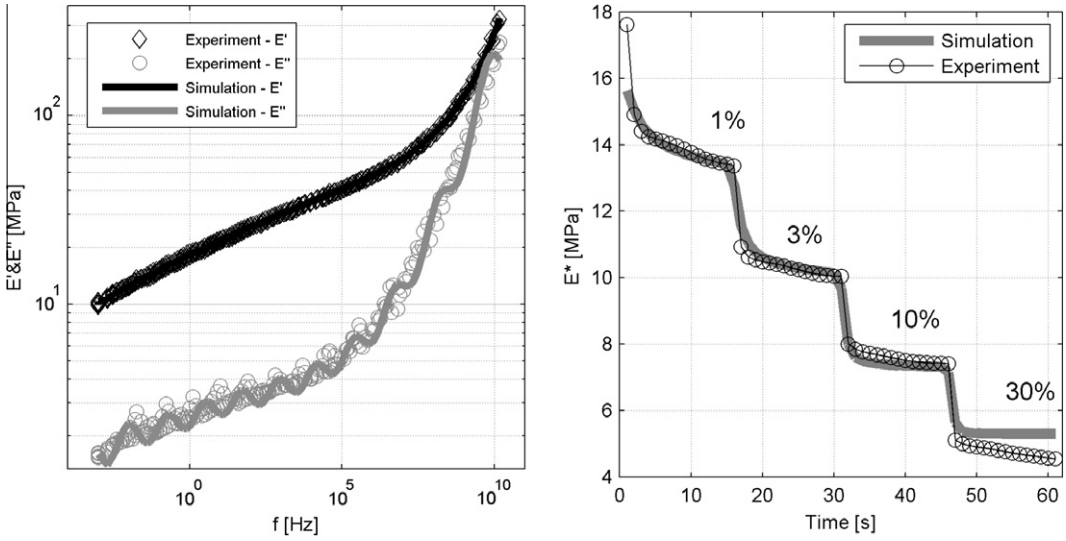

Fig. 14. Identification process for 12 Maxwell elements: identification of the parameters c_k, η_k describing the frequency dependence and static stiffness $4\partial^2\psi_{eq}/\lambda_0\partial\mathbf{C}^2|_{\lambda_0}$ describing the equilibrium behaviour (L); identification of the amplitude- and time dependent material parameters d_k, λ_k (R).

cation implies the solution of a nonlinear least-squares problem with optimization:

$$\min_{\mu,\eta_k,c_k,d_k,\lambda_k} \frac{1}{2}\left\|\mathbf{E}'_{\mathrm{OPT}}\right\|_2^2 = \frac{1}{2}\sum_i \left(\mathbf{E}'_{\mathrm{DMA}}(\omega_i) - \mathbf{E}'_{\mathrm{SIM}}(\omega_i)\right)^2 \tag{86}$$

For quantitative sufficient parameter identification results with numerical values of the residual norm below 0.1% only 12 nonlinear Maxwell elements were needed. The parameters are listed in Table 2. Since the quality of the approximation is sufficient it is not necessary to incorporate more Maxwell elements and hence more material parameters into the constitutive model.

If the frequency range of interest which is relevant for a given technical application is smaller, a smaller number of Maxwell elements are needed to represent the experimental data. To reduce the waviness of the simulated loss modulus curve, a larger number of Maxwell elements should even be used. We made good experience with about three Maxwell elements per decade in the frequency range but this leads to a pronounced increase in the computing time. For these reasons, the number of Maxwell elements which is used to represent the material behaviour is always a compromise between accuracy and computing time. In this paper, 12 Maxwell elements were used to describe the material behaviour over 15 decades in the frequency domain. If the dynamic behaviour of a real elastomer structure should be simulated with FEM, for example in the frequency range between 1 Hz and 20 Hz, then three Maxwell elements are sufficient. But in this case, the parameters of the elements have to be identified anew such that the storage and loss moduli in Fig. 14 L are approximated only in this range.

Table 2
Identified material parameters of filled ESBR with 50 phr carbon black (12 nonlinear Maxwell elements).

$4\partial^2\psi_{eq}/\lambda_0\partial\mathbf{C}^2\|_{\lambda_0} = 2.84$		$d = 0.001$ (near incompressible)	
c_k (MPa)	η_k (MPa s)	λ_k (s)	d_k (–)
$c_1 = 3.2825$	$\eta_1 = 0.0791$	$\lambda_1 = 208.0396$	$d_1 = 9.5834$
$c_2 = 1.4997$	$\eta_2 = 2.3326$	$\lambda_2 = 11.1762$	$d_2 = 28.9479$
$c_3 = 2.4369$	$\eta_3 = 0.4517$	$\lambda_3 = 111.6479$	$d_3 = 11.3158$
$c_4 = 0.7705$	$\eta_4 = 0.1427$	$\lambda_4 = 96.6838$	$d_4 = 6.6054$
$c_5 = 4.5348$	$\eta_5 = 0.0086$	$\lambda_5 = 245.4763$	$d_5 = 11.8292$
$c_6 = 5.6670$	$\eta_6 = 0.0009$	$\lambda_6 = 394.8773$	$d_6 = 25.9584$
$c_7 = 1.7240$	$\eta_7 = 123.57$	$\lambda_7 = 1.1461$	$d_7 = 170.413$
$c_8 = 1.3004$	$\eta_8 = 2.0097$	$\lambda_8 = 3.1922$	$d_8 = 18.3577$
$c_9 = 1.4179$	$\eta_9 = 421.45$	$\lambda_9 = 1.1362$	$d_9 = 703.421$
$c_{10} = 0.988$	$\eta_{10} = 0.011$	$\lambda_{10} = 188.54$	$d_{10} = 8.1464$
$c_{11} = 1.377$	$\eta_{11} = 1265$	$\lambda_{11} = 1.0000$	$d_{11} = 999.99$
$c_{12} = 2.427$	$\eta_{12} = 25.31$	$\lambda_{12} = 2.7444$	$d_{12} = 138.61$

6. FEM simulation of cyclic loaded parts under constant preload

6.1. Rubber block loaded with harmonic displacement with stepwise changing dynamic amplitude

To illustrate the properties and the main benefits of presented material model, transient FEM simulations of a rubber block with a hole in the centre were carried out.

Such a part could be used, for example, as an engine vibration isolator. The bottom plate is fixed in all directions. The top plate moves in the vertical *Y*-direction with a transient displacement function with changing dynamic amplitudes (Fig. 15-L). The static preload is 20% in tension and the excitation frequency of 1 Hz. The displacement amplitude was switched three times, every 25 s during the computation time corresponding to 1%, 5%, 10% and 15% global dynamic strain amplitude. The material parameters of the 12 nonlinear Maxwell elements for this simulation were identified in Section 5 (Table 2) and contain all information about the material including time reduction. Total computation time of the FEM simulation is reduced by the same scaling factor as used in the identification procedure. Thus, the FEM simulation of about 100 s duration corresponds to a real loading process of 180×100 s. Looking at the stress response (Fig 16-L) of a given material point of the rubber block with the hole, the experimentally observed softening effect from the DMA test (Fig. 6) is represented by the constitutive model.

For the purpose of an easier post-processing and a well-defined physical understanding of the dynamic behaviour of the block, the dynamic modulus was computed on the basis of the stress signal scaled with the amplitude of the local strains $\Delta\varepsilon$ (Fig. 17). The curve of the time-dependent dynamic modulus shows the expected stepwise decrease with increasing dynamic strain amplitude. This result corresponds to the Payne-effect in the time domain and was observed in the DMA step-tests plotted in Fig. 9.

The effect of different microstructural relaxation times during the different deformation amplitudes can be seen by the simula-

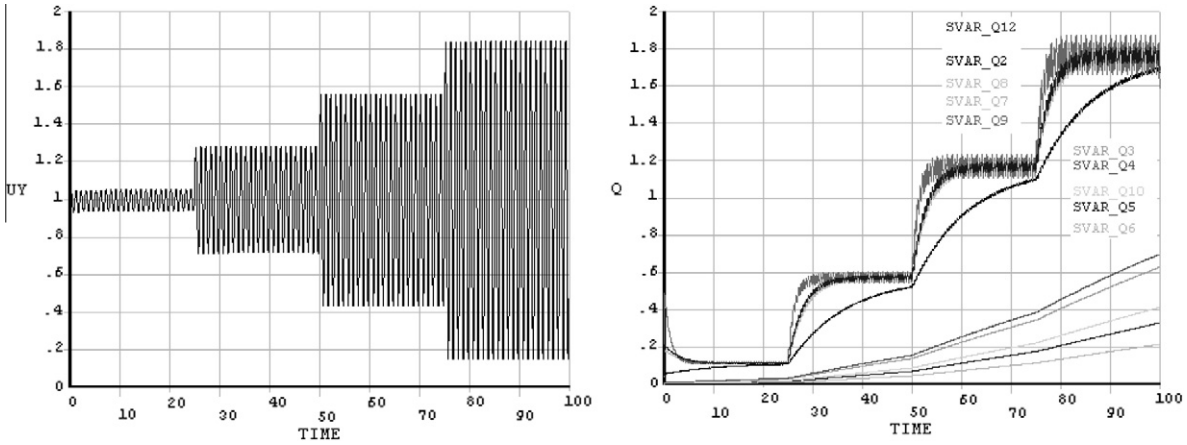

Fig. 15. Displacement-controlled loading function (L) and internal state variables $q_k(t)$ at each Maxwell element (R).

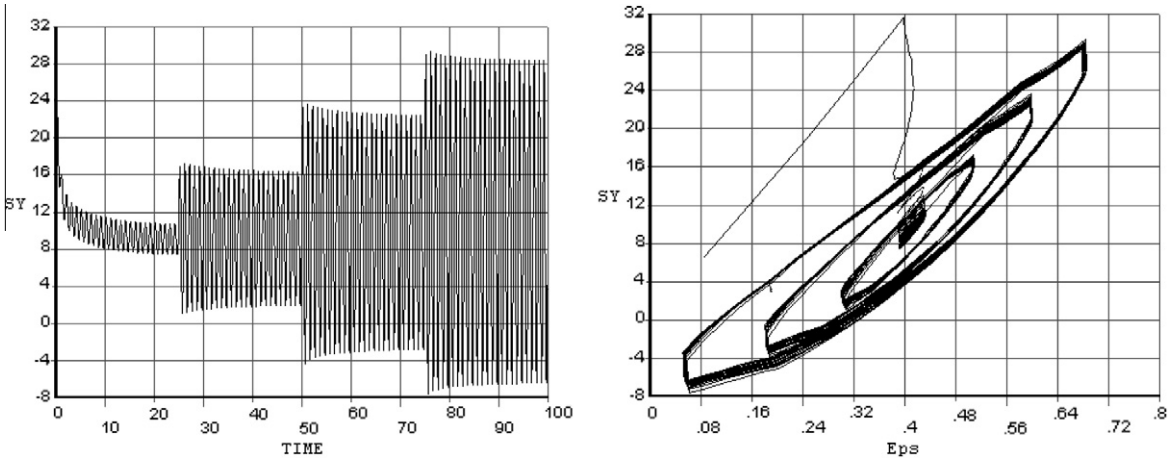

Fig. 16. Stress in *Y*-direction in the hole-area of the part (L); corresponding hysteresis loops (R).

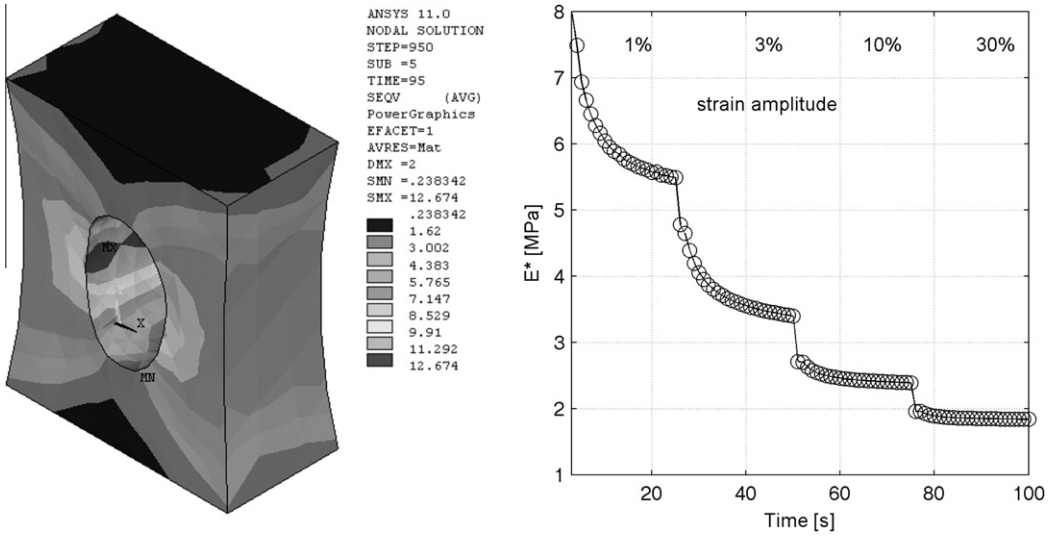

Fig. 17. Stress allocation on the part (L); computed dynamic modulus in the hole-area (R).

tions too (Fig. 17-R). The positions of critical strains and stresses in the rubber block can be detected directly in the post-processor because the local dynamic modulus is influenced by these quantities (Fig. 17-L). As a matter of fact, the area around the hole of the rubber block is the most critical location. According to the computed modulus in Fig. 17-R, the local stiffness is about four times smaller during large cyclic deformations than during small ones. This knowledge can be supportively used in the context of material or

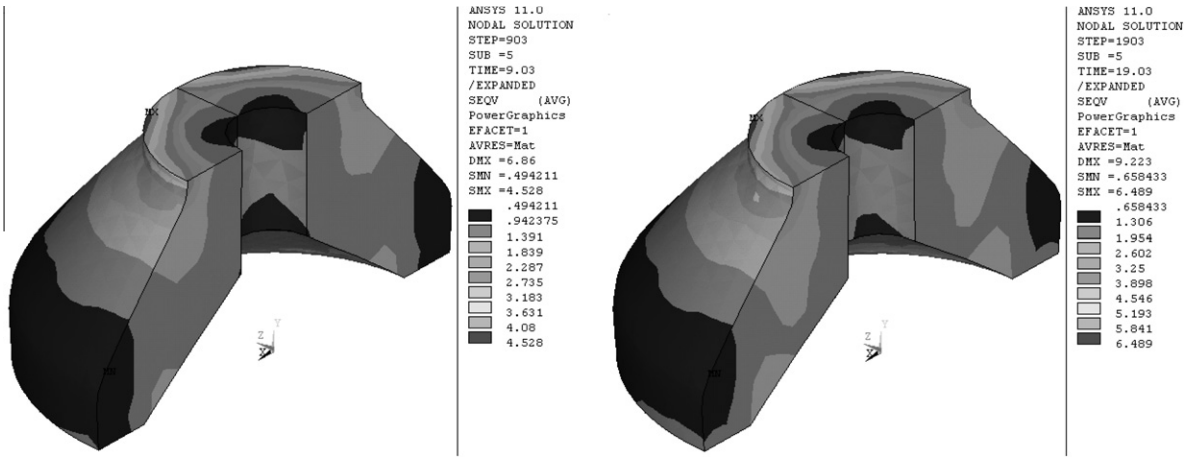

Fig. 18. Maximum Mises stress, allocation at 1 Hz (L) and at 10 Hz (R).

shape optimizations of bushings or shock elements. Further applications of transient simulations can be found in the big area of multibody simulation in the automotive industry. In this context, the dynamic reaction forces from suspension bushings or engine mounts contain basic information for further works, like durability or NVH analyses.

6.2. Shock absorber loaded with harmonic displacement with stepwise changing frequency

In the following example, the stress response of a shock absorber under vibrations of the engine, during which the rotation speed changes, was computed. This process is simulated with a sinusoidal displacement-controlled excitation under compression with a changing frequency from 1 Hz to 10 Hz after 10 s. Since the weight of the engine induces a preload to the shock absorber, a static preload of 6% is superimposed to the harmonic load with 3% amplitude. These values are related to the height of the shock absorber in the undeformed state. The material parameters are the same as in the simulation above. The displacement-controlled dynamic excitation and the simulated frequency-dependent stress response at a given location of the shock absorber are plotted in Fig. 19. A pronounced relaxation of the mean stress and a superimposed change in the stress amplitude is observed. In the case of the smaller frequency of 1 Hz, the relaxation of the mean stress is faster and the stress amplitude is smaller than in the case of the higher frequency of 10 Hz. This indicates the stiffening of the material with growing frequency as observed in the frequency sweep tests (Fig. 14). Fig. 18 depicts the stationary Mises stress distribution at the time of 9 s under 1 Hz and at 19 s under an excitation frequency of 10 Hz.

7. Conclusions

- To investigate both the stationary and the transient nonlinearities of the dynamic modulus in the context of the Payne-effect comprehensive DMA-experiments were carried out. In order to separate the Mullins-effect from the effects of interest a conditioning of specimens with a mechanical deformation process was applied. The conditioning process is a strain-controlled amplitude sweep test with sufficient high maximum amplitude (equal to or larger than the maximum strain amplitude in the experiments of interest). During the DMA tests, the time-dependent force and elongation signals were recorded and post-processed by standard methods. In the case of filler-reinforced rubber, the stress signals are strongly influenced by the amplitude-history of the deformation input. Standard DMA-experiments under stationary conditions, i.e. under constant strain amplitude and frequency, are sufficient to quantify the amplitude dependence of filled elastomers. But they are not sufficient to study the transient behaviour of the material, for example under increasing or decreasing amplitude jumps. To study this behaviour, multi-step experiments with stepwise changing strain amplitudes were run. The corresponding stress–strain

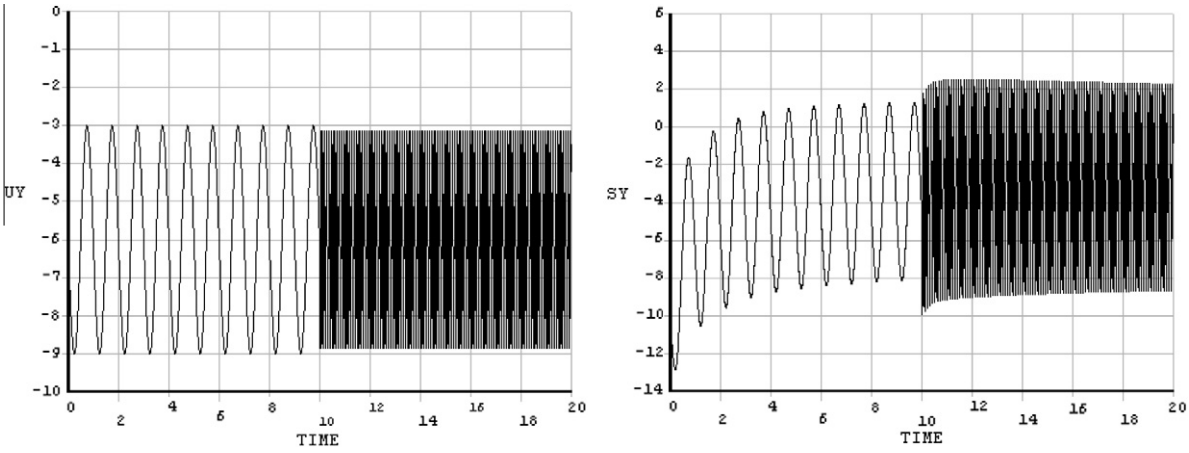

Fig. 19. Displacement loading function (L); *Y*-component of the stress response in the critical area (R).

hysteresis loops clearly exhibit the amplitude dependence: changes in the strain amplitude lead to pronounced changes in the mean stiffness of the stress–strain curves. In the case of spontaneous strain amplitude changes, it is observed that the dynamic modulus is not constant but exhibits a time-dependent behaviour. This can be explained by microstructural relaxation effects.

- With the knowledge about the material behaviour of filled reinforced rubber in the mind, a new constitutive model of finite viscoelasticity which is motivated by rheological elements was developed. The formulated model is thermodynamically consistent and provides a good basis for modelling thermodynamic effects in future projects. In the case of elastomers, the dissipative heating can also be modelled; see, e.g. Lion (1997), Luo et al. (2005) and Rendek and Lion (2008). More details about the simulation of dissipative heating-up processes and the proof of the thermodynamical consistency of the model are discussed in Rendek and Lion (2010). Considering the concept of internal state variables, the experimentally observed nonlinearities like amplitude dependence and microstructural relaxation are modelled. The formulation of the constitutive equations was oriented with regard to an efficient and simple FEM implementation. The solution procedure, implemented into the FEM-program ANSYS, was used to solve the differential equations of the constitutive model in the context of boundary value problems.
- To implement the constitutive equations into the FEM code ANSYS a new implementation framework connected to the interface of the subroutine USERMAT was developed. In this framework, the updates of the stress tensor and the tangent operator were at first computed in the current configuration with respect to a material reference frame. Then, they were transformed to the new rotated frame.
- For FEM simulations of real parts, the underlying material must be characterised. To develop an efficient parameter identification process, the constitutive model was transformed to the frequency domain. This is only admissible under special assumptions but provides the possibility to carry out the identification in both the time and the frequency domain. In the case of the identification in the frequency domain, the identified parameters allow to describe the material behaviour in a fairly wide range of frequencies and amplitudes. In the time domain, this is only possible with an enormous amount of computation time. Finally, some transient FEM simulations were carried out in order to demonstrate the ability of the constitutive model to describe the dynamic behaviour of real structures.

Acknowledgements

Parts of this research are financially supported by the German Research Foundation (DFG). The technical support provided by Prof. Dr.-Ing. Armin Fritsch in the context of the finite element implementation is gratefully acknowledged.

References

Amin, A.F.M.S., Lion, A., Sekita, S., Okui, Y., 2006. Nonlinear dependence of viscosity in modeling the rate-dependent response of natural and high damping rubbers in compression and shear: experimental identification and numerical verification. International Journal of Plasticity 22, 1610–1657.

ANSYS, 2007. Programmer's Manual for ANSYS (ANSYS Release 11.0), p. 312.

Baris, A.N., Edwards, B.J., 1993. On the admissibility criteria for linear viscoelasticity kernels. Rheoiogica Acta 32, 505–510.

Bokobza, L., 2009. New developments in rubber reinforcement. KGK – Kautschuk Gummi Kunststoffe (01–02), 23–27.

Bonet, J., Wood, R.D., 1997. Nonlinear Continuum Mechanics for Finite Element Analysis. Cambridge University Press, Cambridge, MA.

Buche, F., 1961. Mullins effect and rubber–filler interaction. Journal of Applied Polymer Science 4 (15), 271–281.

Coja, M., Kari, L., 2005. Rubber versus steel vibration isolators. KGK – Kautschuk Gummi Kunststoffe, 564–569.

Coleman, B.D., 1961. Foundation of linear Viscoelasticity. Reviews of Modern Physics 33 (2), 239–249.

Crisfield, M.A., 1997. Non-linear Finite Element Analysis of Solids and Structures, vol. 2, Advanced Topics, Wiley, Chichester, UK.

Crisfield, M.A., 1998. Non-Linear Finite Element Analysis of Solids and Structures. Wiley, Chichester, UK.

Dorfmann, A., Be'ersheba, I., 1995. Fractional differential models in finite viscoelasticity. Acta Mechanica 124, 155–180.

Ehlers, W., 1999. Vektor-und Tensorrechnung Eine Einführung. Stuttgart, Universität Stuttgart, 51.

Felippa, C.A., 2000. A Systematic Approach to the Element-Independent Co-Rotational Dynamics of Finite Elements, Department of Aerospace Engineering Sciences and Center for Aerospace Structures, Boulder, Colorado, University of Colorado, Report No. CU-CAS-00-03.

Garcia, M.J., 2006. Engineering Rubber Bushing Stiffness Formulas Including Dynamic Amplitude Dependence, Department of Aeronautical and Vehicle Engineering. Stockholm, Royal Institute of Technology, Master, 33.

Govindjee, S., Simo, J., 1992. Transition from micro-mechanics to computationally efficient phenomenology: carbon black filled rubbers incorporating Mullins effect. Journal of the Mechanics and Physics of Solids 40 (1), 213–233.

G'Sell, C., Jonas, J.J., 1981. Yield and transient effects during the plastic deformation of solid polymers. Journal of Materials Science 16 (1981), 1956–1974.

Hardwood, J.A.C., Mullins, L., Payne, A.R., 1965. Stress softening in natural rubber vulcanizates. Part II. Stress softening effects in pure gum and filler loaded rubbers. Journal of Applied Polymer Science 9, 3011–3021.

Hartman, S., 2003. Finite-Elemente Berechnung inelastischer Kontinua (Interpretation als Algebro – Differentialgleichungssysteme) Institut für Mechanik Kassel, Kassel, Universität Kassel, Habilitationsschrift, 193.

Hartman, S., Haupt, P., 1999. Spannungsalgorithmus zur Berücksichtigung nichtlinearer Viskoelastizität. Projekt H 20329 Continental AG Hannover_ Kassel Institut für Mechanik. Universität Gesamthochschule Kassel 56.

Hasanpour, K., Ziaei-Rad, S., Mahzoon, M., 2009. A large deformation framework for compressible viscoelastic materials: constitutive equations and finite element implementation. International Journal of Plasticity 25, 1154–1176.

Haupt, P., 2000. Continuum Mechanics and Theory of Materials. Springer, Berlin.

Haupt, P., Lion, A., 2002. On finite linear viscoelasticity of incompressible isotropic materials. Acta Mechanica 159 (2002), 87–124.

Heinrich, G., Klüppel, H., 2004. The role of polymer-filler-interphase in reinforcement of elastomers. KGK – Kautschuk Gummi Kunststoffe 57 (9/2004), 452–454.

Hoefer, P., Lion, A., 2009. Modelling of frequency- and amplitude-dependent material properties of filler-reinforced rubber. Journal of the Mechanics and Physics of Solids 57 (2009), 500–520.

Holzapfel, G.A., 1996. On large strain viscoelsticity: continuum formulation and finite element applications to elastomeric structures. International Journal for Numerical Methods in Engineering 39 (1996), 3903–3926.

Hossain, M., Possart, G., Steinmann, P., 2008. A small-strain model to simulate the curing of thermosets. Computational Mechanics 43 (6), 769–779.

Hossain, M., Possart, G., Steinmann, P., 2009. A finite strain framework for the simulation of polymer curing. Part I: elasticity. Computational Mechanics 44 (5), 621–630.

Hughes, T.J.R., Wingets, J., 1980. Finite rotation effects in numerical integration of rate constitutive equations arising in large-deformation analysis. International Journal for Numerical Methods in Engineering 15, 1862–1867.

Ji-Hyun Cho, S.-K.Y., 2006. A viscoelastic constitutive model of rubber under small oscillatory load superimposed on large static deformation considering the Payne effect. Archive of Applied Mechanics 75 (2006), 275–288.

Kaliske, M., Rothert, H., 1997. On the finite element implementation of rubber-like materials at finite strains. Engineering Computations 14 (1997), 216–232.

Khan, A., Lopez-Pamies, O., 2002. Time and temperature dependent response and relaxation of a soft polymer. International Journal of Plasticity 18, 1359–1372.

Kraus, G., 1966. Stress softening in carbon black-reinforced vulcanizates. Strain rate and temperature effects. Journal of Applied Polymer Science 10, 229–244.

Krawietz, A., 1986. Materialtheorie: Mathematische Beschreibung des Phenomenologischen Thermomechanischen Verhaltens. Springer, Berlin.

Laiarinandrasanaa, L., Piquesa, R., Robisson, A., 2003. Visco-hyperelastic model with internal state variable coupled with discontinuous damage concept under total Lagrangian formulation. International Journal of Plasticity 19, 977–1000.

Lion, A., 1996. A constitutive model for carbon black filled rubber: experimental investigations and mathematical representation. Continuum Mechanics and Thermodynamics 8 (1996), 153–169.

Lion, A., 1997. A physically based method to represent the thermomechanical behaviour of elastomers. Acta Mechanica 123 (1997), 1–26.

Lion, A., 2000. Thermomechanik von Elastomeren: Experimente und Materialtheorie, Institut für Mechanik Kassel Gesamthochschule Kassel, Habilitationsschrift, 228.

Lion, A., 2004. Phenomenological modelling of the material behaviour of carbon black-filled rubber in continuum mechanics. KGK – Kautschuk Gummi Kunststoffe 57 (4/2004), 184–190.

Lion, A., 2005. Phenomenological modelling of strain-induced structural changes in filler-reinforced: elastomers – a time domain formulation of Kraus model. KGK – Kautschuk Gummi Kunststoffe 58 (4/2005), 157–162.

Lion, A., Kardelky, C., 2004. The Payne effect in finite viscoelasticity: constitutive modelling based on fractional derivatives and intrinsic time scales. International Journal of Plasticity 20, 1313–1345.
Lion, A., Retka, J., Rendek, M., 2009. On the calculation of predeformation-dependent dynamic modulus tensors in finite nonlinear viscoelasticity. Mechanics Research Communications 36, 653–658.
Liu, M., 2007. A Three-Dimensional Hyper-Viscoelasticity Constitutive Model for the Dynamic Response Of Rubber, The Graduate Faculty of The University of Akron, Akron, The University of Akron, Master, 110.
Lubliner, J., 2006. Plasticity Theory, Pearson Education, Inc.
Luo, R.K., Wu, W.X., Mortel, W.J., 2005. In: Real Time Simulation and Testing on Heat Generation of Rubber Spring Under Dynamic Loading Fourth European Conference for Constitutive Models for Rubber, ECCMR 2005, Stockholm, Sweden A.A. Balkema Publishers.
Menard, K.P., 1999. Dynamical Mechanical Analysis: A Practical Introduction. CRC Press LLC, New York.
Middendorf, P., 2001. Geometrisch nichtlineare Viscoelastizität, Munich.
Miehe, C., Keck, J., 2000. Superimposed finite elastic–viscoelastic–plastoelastic stress response with damage in filled rubbery polymers. Experiments, modelling and algorithmic implementation. Journal of the Mechanics and Physics of Solids 48 (2000), 323–365.
Müller, I., 1973. Thermomechanik: Die Grundlagen der Materialtheorie, Bertelsmann Universitätsverlag.
Mullins, L., Tobin, N.R., 1965. Stress softening in rubber vulcanizates. Part I. Use of a strain amplification factor to describe the elastic behavior of filler-reinforced vulcanized rubber. Journal of Applied Polymer Science 9, 2993–3009.
Ouyang, G.B., 2006. Modulus, hysteresis and the payne effect: network junction model for carbon black reinforcement. KGK – Kautschuk Gummi Kunststoffe (06), 332–343.
Payne, A.R., 1962a. The dynamic properties of carbon black-loaded natural rubber vulcanizates. Part I. Journal of Applied Polymer Science VI (19), 57–63.
Payne, A.R., 1962b. The dynamic properties of carbon black-loaded natural rubber vulcanizates. Part II. Journal of Applied Polymer Science VI (21), 368–372.
Payne, A.R., 1965. Dynamic properties of natural rubber containing heat-treated carbon blacks. Journal of Applied Polymer Science 9 (1965), 3245–3254.
Payne, A.R., Whittaker, R.E., 1972. Effect of vulcanization on the low-strain dynamic properties of filled rubbers. Journal of Applied Polymer Science 16 (1972), 1191–1212.
Ramorino, G., Ricco, T., 2003. Developments in dynamic testing of rubber compounds: assessment of non-linear effects. Polymer Testing 22, 681–687.
Reese, S., Govindjee, S., 1998. A theory of finite viscoelasticity and numerical aspects. International Journal of Solids and Structures 35, 3455–3482.
Rendek, M., Lion, A., 2008. Amplitude- and temperature effects of filler-reinforced rubber: experiments and modelling. PAMM 8 (1), 10457–10458.
Rendek, M., Lion, A., 2009. Finite-Elemente-Berechnung dynamischer Eigenschaften von Elastomeren. DVM – Tag 2009 Elastomerbauteile, Berlin (Germany), DVM.
Rendek, M., Lion, A., 2009b. Modelling and finite element simulation of filler-reinforced elastomers under dynamic deformations. KGK – Kautschuk Gummi Kunststoffe, 28–35.
Rendek, M., Lion, A., 2010. Strain induced transient effects of filler reinforced elastomers with respect to the Payne-effect: experiments and constitutive modelling. Journal of Applied Mathematics and Mechanics 90 (5), 436–458.
Robertson, C.G., Wang, X., 2005. Isoenergetic jamming transition in particle-filled systems. Physical Review Letters 95, 703–707.
Robertson, C.G., Wang, X., 2006. Spectral hole burning to probe the nature of unjamming (Payne effect) in particle-filled elastomers. Europhysics Letters 76 (2), 278–284.
Schwarzl, F.R., Zahradnik, F., 1980. The time temperature position of the glass–rubber transition of amorphous polymers and the free volume. Rheologica Acta 19 (2), 137–152.
Sedlan, K., 2001. Viskoelastisches Materialverhalten von Elastomerverkstoffen: Experimentelle Untersuchung und Modellbildung Institut für Mechanik, Kassel, Universität Gesamthochschule Kassel, Dr.-Ing.
Seifert, T., Maier, G., 2008. Consistent linearization and finite element implementation of an incrementally objective canonical form return mapping algorithm for large deformation inelasticity. International Journal for Numerical Methods in Engineering 75, 690–708.
Seifert, T., Schenk, T., Schmidt, I., 2006. Efficient and modular algorithms in modeling finite inelastic deformations: objective integration, parameter identification. Computer Methods in Applied Mechanics and Engineering 196, 2269–2283.
Simo, J.C., Huges, T.J.R., 2000. Computational Inelasticity. Springer, New York.
Sjöberg, M., 2002. On dynamic properties of rubber isolators, Department of Vehicle Engineering, Stockholm Royal Institute of Technology.
Souza, R.M. d. (2000). Force-based Finite Element for Large Displacement Inelastic Analysis of Frames, Graduate Division of the University of California Berkley University of California, Doctor of Philosophy.
Sullivan, J.L., Demery, V.C., 1982. The nonlinear viscoelastic behavior of a carbon-black-filled elastomer. Journal of Applied Polymer Science 20, 2083–2101.
Suwannachit, A., Nackenhorst, U., 2010. On the constitutive modeling of reinforced rubber in a broad frequency domain. Journal of Applied Mathematics and Mechanics 90 (5), 418–435.
Veubeke, B.M.F.d., 1976. The dynamics of flexible bodies. International Journal of Engineering Science 56, 1976.
Williams, M., Landel, R., Ferry, J.D., 1955. The Temperature Dependence of Relaxation Mechanisms in Amorphous Polymers and Other Glass-forming Liquids, Department of Chemistry, University of Wisconsin, pp. 3701–3707.
Wrana, C., Härtel, V., 2008. Dynamic mechanical analysis of filled elastomers. KGK – Kautschuk Gummi Kunststoffe (12/2008), 647–655.
Wrana, C., Eisele, U., Kelbch, S., 2000. Measurement and molecular modeling of rolling resistance in tire treads. KGK – Kautschuk Gummi Kunststoffe 53 (3/2000), 126–128.